This file was generated for the first submission to JPO on September 17, 2015.
It is subject to change. Please email me or go to AMS website for the final version.
- Jinbo Wang

Cross-stream transport near the Drake Passage

Jinbo Wang * Matthew R. Mazloff, Sarah T. Gille

Scripps Institution of Oceanography, California University San Diego, La Jolla, CA, USA

Marie-José Messias, Andrew Watson

School of Environmental Sciences, University of East Anglia, Norwich, UK

James R. Ledwell

Woods Hole Oceanographic Institution, Woods Hole, Massachusetts, USA

* *Corresponding author address:* 9500 Gilman Dr. #0230, La Jolla, CA, 92093, USA

E-mail: jinbow@alum.mit.edu

ABSTRACT

Cross-stream transport plays an important role in the Southern Ocean. In this paper, the local process of cross-stream transport near the Drake Passage, Scotia Sea and adjacent regions is studied using particle simulations in a Southern Ocean State Estimate (SOSE) and the measurements of the tracer release experiment conducted during the Diapycnal and Isopycnal Mixing Experiment in the Southern Ocean (DIMES). The DIMES tracer was released in the southeast Pacific within the Antarctic Circumpolar Current between the Subantarctic Front and Polar Front. Particle simulations in SOSE are statistically consistent with DIMES tracer evolution. SOSE particles and DIMES tracer measurements both show a robust poleward drift from the initial point release. The poleward drift occurs mainly within several "leaky jet" regions associated with topographic transitions, where jets diverge and particle trajectories bifurcate. These regions include the Shackleton Ridge, the fracture zones in the Scotia Sea, the North Scotia Ridge, and the Falkland Plateau. Numerical particles released along a depth-latitude section at 110°W show that a pattern of classic Southern Ocean Meridional Overturning Circulation (SOMOC), with poleward transport sandwiched between the 27.6 and 28.0 neutral density levels, emerges only after particles pass through the "leaky jets", indicating the importance of local dynamics in the Drake Passage and Scotia Sea area in forming the zonally integrated SOMOC.

1. Introduction

The Southern Ocean supports an energetic Antarctic Circumpolar Current (ACC), which is composed of several narrow fronts characterized by swift currents and steep isopycnals. The ACC frontal structure is shaped by the combined effect of strong westerlies, air-sea buoyancy fluxes, and the fact that ACC follows a circumpolar path, unbroken by continental boundaries. While the outcropping of isopycnals in the ACC supports deep ocean ventilation, it also generates a strong potential vorticity gradient that tends to inhibit poleward tracer transport and shield the Antarctic region from the direct influence of the subtropics. The connectivity between low latitudes and high latitudes, and the associated tracer transport, are crucial aspects of the Earth's climate system (Marshall and Speer 2012). In this paper, we study the cross-stream transport in the Southern Ocean with a focus on the Drake Passage region.

Both the zonally-averaged view and local analyses are important for understanding the cross-ACC transport. In a zonally-averaged view, tracers are advected by the Southern Ocean Meridional Overturning Circulation (SOMOC), which consists of two counter-rotating cells: a clockwise upper cell and a counter-clockwise lower cell (Lumpkin and Speer 2007). The two cells are wind-driven, resulting in the poleward and upward transport of Circumpolar Deep Water that originated as North Atlantic Deep Water or as other deep waters formed from diapycnal mixing. While the zonally-averaged SOMOC is conceptually simple, it masks out the importance of local dynamics, which have been demonstrated to be important for the energy budget, cross-frontal transport, and watermass formation and transformation in the Southern Ocean (Gille 1997; Naveira Garabato et al. 2011; Sallée et al. 2010; Thompson and Sallée 2012; Thompson and Naveira Garabato 2014; Abernathey and Cessi 2014).

The importance of local dynamics for the SOMOC stems from the central role that topography plays in the Southern Ocean. In the zonally-averaged view, the SOMOC is a residual circulation arising from an imbalance between the eddy-induced circulation and wind-driven Eulerian circulation (Johnson and Bryden 1989; Marshall and Radko 2003).

This mechanism is clear in idealized flat-bottom channel models (Abernathey et al. 2011), where transient eddies can be unambiguously separated from the mean by a time- and zonal-averaging operator. However, zonal asymmetry can emerge in response to any along-stream variations in bottom topography (Thompson and Sallée 2012). Bottom topography steers the ACC meanders and modulates eddy generation. In an idealized numerical simulation of a two-layer channel flow over topography, MacCready and Rhines (2001) showed that eddy fluxes are enhanced downstream of a meridional topographic ridge. The ridge enhances the onset of the baroclinic instability and reduces the sensitivity of the zonal transport to external forcing. The ridge also generates a standing eddy, which is defined as the zonal deviation of a time-mean field. This standing eddy is associated with an enhanced local buoyancy gradient, which increases the efficiency of cross-stream transport by transient eddies (Abernathey and Cessi 2014). These topographically-enhanced eddy fluxes are potentially associated with localized hot-spots of upwelling, subduction and watermass transformation (Sallée et al. 2010; Hallberg and Gnanadesikan 2006; Naveira Garabato et al. 2007). Thus local dynamics are needed to explain the three dimensional circulation of the Southern Ocean.

The Drake Passage (DP) and the adjacent area have some of the most dramatic topographic features of the Southern Ocean. The region is associated with an elevated topographic form stress that is important for the ACC momentum balance (Munk and Palmen 1951; Gille 1997). The topography of the region also helps to generate internal waves, leading to enhanced diapycnal mixing (St. Laurent et al. 2012; Sheen et al. 2013; Watson et al. 2013). Similarly local enhancement is also identified in the cross-stream eddy transport. Using Lagrangian particles, Thompson and Sallée (2012) found that cross-frontal exchange is significantly enhanced near and downstream of the DP, Scotia Sea and other major topographic obstacles. The Lagrangian particles used in their study were advected by altimetry-derived velocities at the surface and by velocities from a two-layer quasi-geostrophic model. While their results suggest topographic enhancement of cross-frontal transport, they are limited to the surface and to an idealized layer model.

In this study, we investigate cross-stream exchange near the DP region by combining in situ ocean measurements from the Diapycnal and Isopycnal Mixing Experiment in the Southern Ocean (DIMES) and particle simulations in a Southern Ocean State Estimate (SOSE). The DIMES project was designed to study diapycnal and isopycnal mixing by conducting anthropogenic tracer and subsurface float experiments together with in-situ CTD and microstructure measurements (Gille et al. 2007; Ledwell et al. 2011; Gille 2012; St. Laurent et al. 2012; Watson et al. 2013). We briefly review the DIMES project and the data used in this study in Section 2a. The number of bottle samples of the tracer are large by an operational standard, but still insufficient for a robust quantification of isopycnal spreading. We then use more than one million particles advected in SOSE to simulate the DIMES tracer and to study cross-frontal transport. The methodology is presented in Section 2 and in Appendices A and B. In Section 3, the tracer evolution in the real ocean and in SOSE are directly compared, and we confirm that the tracer simulation agrees well with the DIMES tracer measurements. After validating and analyzing the SOSE particle simulation, an additional experiment is done to study the vertical structure of the cross-stream exchange by releasing particles along a latitude-depth section at 110°W. These results, presented in Section 4 show that the DP and Scotia Sea regions are associated with enhanced cross-stream exchanges and that Circumpolar Deep Water experiences poleward transport within the DP/Scotia Sea longitude. Conclusions are given in Section 5.

2. Methodology

a. Data: DIMES tracer measurements

To investigate diapycnal and isopycnal mixing in the Southern Ocean near the DP, 76 kg of trifluoromethyl sulphur pentafluroide (CF_3SF_5) were released on the 27.906 kg m^{-3} neutral density surface in an X-shaped pattern consisting of two 20-km-long streaks near 58.1°S, 106.7°W (Ledwell et al. 2011). The location is marked in Figure (1, left) by the black dot-cross symbol. This stagnant region was deliberately chosen to ensure that the tracer was not swept away quickly by ACC fronts (colors in Fig. 1, left). The in-situ CTD T/S measurements indicated that this location is between the Subantarctic Front (SAF) and the Polar Front (PF). More detailed descriptions are provided by Ledwell et al. (2011), by Tulloch et al. (2014), and in the DIMES cruise reports from dimes.ucsd.edu.

For this study, we make use of seven DIMES cruises carried out over the five subsequent years (Table 1). The locations of CTD station and tracer sampling sites are shown in Figure 2. US2, UK2, UK2.5, and US3 sampled the southeast Pacific and UK3, 4, 5 sampled the DP and the downstream regions. The observed tracer concentrations at various depths are first interpolated onto a uniform vertical grid with 10 m spacing and then column integrated to obtain tracer mass per unit area. In Section 3, we use the column-integrated tracer to validate the SOSE particle simulation.

b. The Southern Ocean State Estimation (SOSE)

We use passively advected synthetic particles to provide a more detailed view of tracer dispersion than that we can obtain from the DIMES in situ tracer alone. The performance of the particle simulation is largely determined by the velocity field. We use the SOSE product, because it is constrained by many observations including a large collection of Argo temperature and salinity profiles and satellite data. SOSE assimilates observational data via an adjoint method minimizing the misfit between the estimation and observations while conserving temperature, salinity, volume and momentum at each step (Mazloff et al. 2010). In this study, we use SOSE iteration-100, which consists of 6 years of daily-averaged data from 2005 to 2010 at 1/6 degree horizontal resolution with 42 vertical levels. An open boundary condition matching the ECCO product of Forget (2010) is applied. The results have been tested in several studies, which have shown, for example, in the DP region, that the vertical structure of the SOSE velocity is consistent with shipboard acoustic Doppler current profiles (Firing et al. 2011).

Figure 3 shows the mean surface dynamic topography (a, b, c) and surface eddy kinetic energy (EKE) (d, f) based on the AVISO data (Archiving, Validation and Interpretation of Satellite Oceanographic Ducet et al. (2000)) (a, d), the Earth Gravity Model 2008 (EGM08) (Pavlis et al. 2012) (b), and SOSE (c, f), in the DP region. In general, the SOSE fields are consistent with AVISO and EGM08 data both in the mean and EKE fields. Several exceptions exist. In the mean field, SOSE does not reproduce the Zapiola anticyclonic gyre (Mazloff et al. 2010), probably due to the inadequate representation of the trapped basin mode in the deep Argentine basin (Weijer et al. 2015). Because the EKE is directly related to eddy effective diffusivity, eddy mixing based on SOSE velocity may be underestimated in the regions where the SOSE EKE is weaker than observations. However, because our focus is south of 50°S, where most of the DIMES tracer measurements were collected, discrepancies near the confluence zone have only modest impact on our analysis.

c. Particle simulation of a point tracer release

Eulerian tracer simulation is the most direct way to reproduce in-situ tracer evolution. However, tracer release in the real ocean is spatially confined, often within a patch smaller than the size of a single model grid cell. Ideally one can increase model resolution to explicitly resolve the initial tracer patch as Tulloch et al. (2014) did. High-resolution numerical simulations, however, are computationally too expensive to be ideal for ensemble statistics. In addition, the direct Eulerian simulation of a point tracer in a coarse-resolution model suffers from artificial numerical noise and spurious numerical diffusion (Griffies 2004).

Alternatively, a tracer patch can be treated as a collection of Lagrangian water parcels. The Lagrangian method has been common practice for studies of evolution of pollutants in the atmosphere (Stohl et al. 2005) and oceans (Terada and Chino 2008; Liu et al. 2011; Mariano et al. 2011) and for investigation of ocean general circulation (Döös et al. 2011; van Sebille et al. 2009, 2012, 2013). While particle simulations also have numerical errors, they have the advantages of theoretically infinitesimal resolution and controllable numerical diffusion. Particles are particularly useful in simulating the transport and dispersion of a point tracer.

In a cloud of particles, each particle carries a portion of the total tracer mass. Let c denote the mass per particle; then the corresponding Eulerian tracer concentration field $C(\mathbf{x}, t)$ can be written as

$$C(\mathbf{x}, t) = \sum_{i=0}^{N} W(\mathbf{x} - \mathbf{x}_i(t))c, \tag{1}$$

where N is the total number of particles, $\mathbf{x}$ is the particle position, and W is a smoothing kernel function that maps the particle density to tracer density and satisfies the normalization condition to conserve mass

$$\int_\Omega W \, \mathrm{d}x \, \mathrm{d}y \, \mathrm{d}z = 1,$$

where Ω is the integral volume in three dimensions. The smoothing kernel W is an essential element in the Smoothed Particle Hydrodynamic approach in fluid simulation (Monaghan 1992). Different forms of W exist with different projection errors. Here we consider passive particles and use a simple box-counting method with Gaussian smoothing (see Appendix A). The Lagrangian model and particle-tracer mapping are extensively discussed in Appendix A and B. The column integrated quantity is easily obtained by disregarding the vertical coordinate, i.e.,

$$\int_A W \, \mathrm{d}x \, \mathrm{d}y = 1,$$

where A represents a horizontal area.

A total of one million particles are used to reproduce the DIMES tracer release. This is sufficient at least for the first three years. The ideal number of particles N for tracer simulation should be $N > 4\pi N_{optm}\mathbf{K}t/\Delta x^2$ (see Eq. A2), where N_{optm} is an empirical optimal number of particles per grid, $\mathbf{K}$ the effective diffusivity, t the elapsed time, and Δx the resolution of the mapped tracer (see Appendix A). While Klocker and Ferrari (2012) have suggested that $\mathcal{O}(10^6)$ particles are essential for particle dispersion calculations, in our study we find that at day 500, 35,000 particles are in fact sufficient to account for 98% of the variance produced by 10^6 particles. The CF_3SF_5 used in the DIMES project has the molar mass 196.005 g/mole. Distributing 76 kg CF_3SF_5 onto 10^6 particles yields 3.8765×10^{-4} mole/particle. The DIMES tracer was released on February 5, 2009, while particles in SOSE start from February 5, 2005. SOSE results show strong variability in seasonal but not inter-annual time scale, so that we expect the month of the year to be more important than the specific year in simulating tracer spreading.

3. Direct comparison of the DIMES tracer with Lagrangian simulations

In this section, the SOSE tracer simulation is directly evaluated against the DIMES tracer measurements. The bottom-middle panel of Figure 3 shows the trajectories of a subset of the particles released along a line at 106.7°W on the neutral density level 27.9 kg m^{-3}. Those released at the DIMES tracer injection location are marked with red lines. The particle trajectories indicate the ocean circulation near DP. All the particles within the ACC travel eastward and pass through the DP. The trajectories become more tightly packed as the particles approach the DP, because the large-scale flow converges towards the DP and diverges meridionally after passing the DP and exiting the Scotia Sea. Particle density is mapped to tracer concentration using the particle mass calculated in the previous section, and directly compared with the DIMES tracer measurements from seven cruises.

In Figure 4, the DIMES tracer measurements are marked as colored dots, and the results of the SOSE simulation are shown as background contours. The two fields share the same units, colorbar, and the elapsed days since their initial release. After one year, the distribution of tracer concentration, both in observations measured by the US2 cruise and in SOSE simulation, shows high spatial heterogeneity. Extremely low and high tracer concentrations are adjacent to each other indicating the presence of tracer filamentation. The spatial distribution of the DIMES tracer is expected to differ substantially from the simulated tracer within the first couple of years, because SOSE does not capture individual eddies. Instead it minimizes the large-scale observation-model mismatch for the full six years.

In the SOSE simulation, almost all of the tracer was in the southeast Pacific upstream of DP at the time of US2 cruise (after about 1 year). In SOSE, particles start to reach the entrance of the DP (defined to be 68.25°W) around day 500. By the time of the UK2 cruise (about 700 days), about 50% of the particles are predicted to have entered DP, and by the UK2.5 (about 800 days) cruise about 70% of the particles have entered DP. The SOSE results suggest that the two cruises sampled almost the middle of the stretched tracer field.

The UK2-observed tracer concentration is more homogeneous near 78°W, to the west of the DP entrance, than at the entrance of the DP near 68°W. This stems from the convergence of the ACC fronts, which occurs upstream of DP. The ACC convergence has a twofold impact. First, the two ACC fronts, the SAF and PF, act as barriers to the cross-frontal transport enclosing the tracer and obstructing the spatial tracer spreading. Second, the confluence of the two fronts generates enhanced lateral shear towards the DP, which can enhance shear-generated filamentation. For the UK2 cruise, the general match of color between dots and contours, especially over the Shackleton Fracture Zone near 58°W, indicates that the rate of simulated particle spreading is consistent with that inferred from observations. Note that the EKE is larger in SOSE than in AVISO in the DP region south of the PF (Figure 3d,f), which may explain why the tracer distribution is more poleward in SOSE than in UK2 measurements.

At the time of the UK2.5 cruise, about 800 days after release, the SOSE simulation shows that a large portion of the tracer is retained near the DP between 80°W and 55°W. Two legs of the UK2.5 cruise surveyed the tail and the leading edge of the tracer field. At the tail near 77°W, tracers are relatively homogeneous, bounded by low concentrations on the edges of the cruise track. The SOSE simulation shows similar characteristics. Even though the instantaneous tracer fields in simulations are not directly comparable to SOSE simulation values, their matched color contours at (80°W, 61°S) suggest that UK2.5 surveyed some tracers trapped in mesoscale eddies. The leg over the Shackleton Fracture Zone observed less tracer than indicated by the SOSE simulation. The discrepancy is due to the spatial heterogeneity in the tracer distribution caused by segmented ACC jets Messias et al. (2015).

The SOSE tracer distribution at the time of UK3 cruise is the best match to the measurements of all the cruises (Figure 4, UK3). A sharp transition in the tracer concentration over the Shackleton Ridge near (56°W, 57°S) occurs both in the SOSE simulation and observations. This is a persistent feature in SOSE simulations, associated with the northward shift of the ACC fronts. In this region, the PF acts as a barrier to cross-frontal transport. The DP at the Shackleton Ridge is a choke point of the ACC, where the SAF and PF can be just one degree apart (Orsi et al. 1995; Sokolov and Rintoul 2009) and sometimes merge (Cunningham and Pavic 2007). After passing this point, the SAF and PF diverge. The SAF meanders northward following the continental slope of South America as the Malvinas Current. The PF, however, does not meander to the north but instead extends eastward. Much of the tracer is bounded by the two fronts and tends to homogenize between the fronts to yield almost uniform tracer distributions as shown in both SOSE simulation and observations (Figure 4, UK3). A large portion of the SOSE tracer is carried by the Malvinas Current northward toward the Brazil-Malvinas confluence, and it returns back to the south after significant mixing (shown in Section 4). The DIMES tracer observed in the Falkland Trough also appears in the SOSE simulation albeit with smaller amplitude.

By the time of UK4 and UK5, the majority of the tracer has exited the DP into the Argentine Basin. SOSE tracer over the Scotia Ridge is consistent with DIMES measurements both in amplitude and in spatial distribution. There is excess SOSE tracer in the Argentine Basin just north of the North Scotia Ridge compared with measurements. This may be caused by under-simulated eddy energy within this region (Figure 3).

In addition to the the visual comparison of the amplitude and horizontal distribution of the two fields in Figure 4, the meridional spreading can be assessed by quantifying the mean tracer distribution in sea surface height (SSH) coordinate, which also indicates ACC front position. The detailed justification of the SSH coordinate is deferred to Section 4. Here the DIMES tracer is binned to the 60-day-time-mean SSH field for each cruise. The SSH data are derived from the AVISO product (Ducet et al. 2000). Because the SOSE SSH field is noisy and does not match the AVISO data, the AVISO SSH is used to provide a single coordinate system for both tracer fields.

The binned tracer in SSH coordinates is shown in Figure 5. In general, SOSE particles reproduces the DIMES tracer in terms of the meridional spreading and amplitude. Both fields show a clear poleward drift of tracer in time. Tracer peaks at certain SSH levels are also robust in both fields. In the next section we show that the poleward drift is associated with the upwelling branch of the SOMOC. The peak values in SSH coordinates are due to the tracer trapping by ACC fronts. However, there are exceptions for the UK3 and UK4, in which the tracer between the -0.1 m and 0.1 m SSH levels is underestimated by the SOSE tracer. The discrepancies in both UK3 and UK4 measurements are associated with the measurements in the Falkland Trough. The ocean circulation in the narrow trough is possibly not well resolved by the SOSE's 1/6 degree model grid.

We carry out additional simulations to evaluate the sensitivity of the SOSE simulation to the initial tracer location, time of the release, and sub-grid parameterization. The DIMES tracer and the re-sampled SOSE tracer concentration are shown in Figure 6.

The degree to which the particle simulations reproduce the observations depends more on dynamical regime than geographic location. Figure 6 shows the sensitivity of the simulation to the particle releasing locations (A, B, C, D) and timing (D1), and the parameterized eddy diffusivity (D2). DIMES tracer was injected at location A (gray). While A was located in a stagnant region in the real ocean during early February 2009, it is in a different dynamical regime in early February 2005 in SOSE. After shifting the release location to B, C, and D in the model, we observe clear changes in the tracer concentration (red, blue and green symbols). Location B is in an ACC jet. The particles released at B travel faster eastward than the particles released at the other three locations, which results in higher tracer concentrations especially for US2. Velocities at C and D are small. The simulated tracer concentrations in these two cases are closer to the observations (Fig. 6, blue and green). In particular, because D is located in a trough, which is similar to the ocean condition during the DIMES tracer injection, case D (green) gives the best simulation of the observations among the four cases (A, B, C, D). These results indicate that the initial dynamical regime is more important for tracer dispersion and evolution than the actual geographic release location. As a result, case D1 (magenta), in which particles are released at the same location but 10 days after case D, shows different results from case D, especially during the first two years (US2, UK2).

Having a background parameterized eddy diffusivity is crucially important for the model to capture the correct tracer dispersion (cyan). Reducing κ_h from 25 m^2 s^{-1} in case D to 0 in case D2 results in an obviously unrealistic tracer simulation. The maximum tracer concentrations in D2 are much larger than the observed ones or the ones in case D, especially for US2. The range of the tracer concentration is also much larger in D2 than in D1. These unrealistic results are due to the lack of sub-grid mixing. Other sensitivity tests with $\kappa = 20, 30, 50$ m^2 s^{-1} do not show changes in tracer amplitude.

To summarize, the SOSE particle simulation reasonably reproduces the horizontal spreading of the DIMES tracer both in amplitude and in spatial distribution. SOSE particles capture the tracer poleward drift and the tracer trapping by fronts. The correspondence between the simulated values and the observations is better during UK2.5 and UK3, due to the fact that the confluence of the ACC limits the tracer spreading and reduces the uncertainties in the spatial variation of the tracer concentration. Even though there is no clear structural association between the simulated and observed tracer fields for US2, both fields show strong heterogeneity. The poleward drift in both datasets is consistent with the zonally averaged SOMOC for this density class. The reasonably good reproduction of the observations by the SOSE simulation gives confidence in the robustness of the statistics and results that are presented in the following sections.

4. Cross-stream transport

Expanding on the work of Thompson and Sallée (2012), who advected virtual particles using altimetry-derived velocities, here we use particles in SOSE to investigate the geographic locations of cross-frontal exchange. We first quantify cross-frontal exchange on the 27.9 neutral density level, and then study the cross-frontal exchange on other density levels. Results show that the DP and the Scotia Sea regions are a vigorous "blender" characterized by an enhanced cross-frontal exchange.

a. Streamline coordinate

Defining a streamline coordinate is the first step in quantifying cross-stream transport. This is a difficult task for the non-stationary and highly segmented ACC. Early studies based on watermass properties along hydrographic sections show that the ACC is composed of three circumpolar fronts, the Subantarctic Front (SAF), the Polar Front (PF) and the southern ACC Front (sACCF) (Orsi et al. 1995; Belkin and Gordon 1996). The ACC fronts vary substantially with longitude. Studies using high-resolution hydrographic sections (Sokolov and Rintoul 2002), satellite data (Gille 1994; Hughes and Ash 2001; Sokolov and Rintoul 2007; Thompson and Sallée 2012), and high-resolution numerical simulations (Hallberg and Gnanadesikan 2006; Thompson et al. 2010) show that ACC fronts lack circumpolar continuity and frequently branch and merge. In addition, major topographic features support stationary meanders that are similar in spatial scale to transient eddies. The lack of eddy-mean scale separation and the heterogeneous characteristics of the ACC fronts introduce ambiguities in the definition of the streamline coordinate. The uncertainty in streamline definition leads to uncertainties in the quantification of cross-stream transport.

A number of recent studies have identified difficulties associated with identifying a robust streamline for analysis (Griesel et al. 2010, 2012; Gille 2014; Chapman 2014; Peña Molino et al. 2014; Dufour et al. 2015). Following numerous previous studies (e.g., Sokolov and

Rintoul 2009), we choose to define streamlines based on SSH contours. Although the ACC is easily defined on the basis of SSH, there is no dynamical reason why the ACC fronts must follow a specific SSH contour. In fact, SSH contours are frequently found to migrate between energetic elongated structures as a result of jet merging and branching (Sallée et al. 2008; Thompson and Sallée 2012). However, the mean SSH is a better coordinate system than temperature or salinity because of its monotonic structure in the meridional direction.

Seasonal variations in SSH could potentially result in seasonal biases in quantities computed relative to time-mean SSH streamline coordinates. We evaluated this by comparing two coordinate systems, one based on the 6-year-mean SSH field and another on the 60-day running-mean SSH field, both from SOSE. We did not find differences that were significant enough to alter our conclusions in the following sections. As an example, Figure 7 shows the trajectory and SSH of a randomly selected particle that was released just south of the DIMES location. The SSH fields are similar overall. The 60-day averaged SSH is more variable than the time-mean SSH, which contrasts with the commonly accepted notion that particles more closely follow contemporaneous rather than time-mean SSH contours. Despite the increased variability, we are able to separate the long-time cross-stream transport from short-time fluctuations by low-pass filtering. Unless otherwise stated, we use the time-mean SSH field as the coordinate system in the following analyses because it is smoother than instantaneous SSH.

The particle trajectory shows the influence of DP on cross-stream transport. The particle starts at SSH level -0.8 m in the southeast Pacific and stays close to this level for about 900 days, then jumps to -0.2 m between 900 and 1100 days (Figure 7). This time period coincides with the particle reaching the entrance of DP where the PF meanders northward toward the SAF. Here the particle enters the SAF and flows into Malvinas Current. The large fluctuations during the time of streamline-crossing indicate the local eddy effect. Similarly, the large fluctuations around day 1250 (Figure 7 top) are due to the eddies in the Brazil-Malvinas confluence zone (orange dots in Figure 7 bottom).

b. *Quantifying cross-stream events*

Let $\psi(X_i(t))$ represent the SSH value along a particle trajectory $X_i(t)$. We define a cross-stream event as a change of ψ larger than 5 cm in five days. We found that changing this criterion affects the absolute number of cross-stream event but leaves the spatial distribution unchanged, as also noted by Thompson and Sallée (2012).

Figure 8 shows an example of the cross-stream events of two randomly chosen particles. Two initially adjacent particles travel in proximity to each other before bifurcating near the DP. Even though the two particle trajectories diverge right after the DP, they eventually converge at the PF in the South Atlantic after about 5 years. Frequent cross-streamline transport occurs near the DP entrance and exit, both between the SAF and PF and near the Malvinas-Brazil confluence (Fig. 9a).

The average direction of the tracer spreading relative to the SSH coordinate is measured by the mean cross-stream transport for all cross-stream events. The point tracer spreads toward lower SSH level, i.e. southward, except for the first 50 days of initial adjustment (Fig. 9b). This southward spreading is consistent with the zonally averaged SOMOC which supports southward transport on the 27.9 neutral density level (Mazloff et al. 2013).

The intensity of the cross-stream exchange is measured by the mean absolute cross-stream transport (Fig. 9c). Enhanced exchange occurs near the DP, consistent with Thompson and Sallée (2012) and Sallée et al. (2011).

c. *Time evolution of the particle Probability Distribution Function in SSH coordinates*

The poleward shift of the particle cloud is clearly shown in the Hovmöller diagrams of the particle probability density function (PDF) in SSH coordinates (Figure 10). The two SSH coordinates, one based on the 6-year-mean (left) and another based on 60-day running mean (right), both reveal the migration of particle clusters toward more negative SSH values. As shown in Figure 7, the SSH of particles is noisier in the 60-day-running mean field, so that the Hovmöller diagram exhibits finer structures and larger cross-stream fluctuations in the 60-day-running mean field than in the 6-year-mean field. Nonetheless, the poleward drift is robust regardless of SSH coordinates. It is consistent with the diagnosis shown in Figure 9b and is especially clear between 500 and 1000 days. The migration is not a gradual process but occurs as jumps from one SSH level to another through time. A dramatic shift occurs between 700 and 800 days, when the center of the particle cloud passes through the DP and Scotia Sea regions.

Particle distributions are not strictly single-Gaussian but have multiple significant peaks not only in SSH coordinates as shown in Figure 10, but also in the zonal and meridional directions (Fig. 11). For example, the particle PDFs in the zonal direction at day 400 and 500 both show significant multi-modal features, an indication of an inhomogeneous eddy field (Fig. 11 top). The PDF in the latitude coordinate cannot be explained by a single-Gaussian function. The bi-modal distribution is shown at day 500 in the latitude coordinate, but is evident at both day 400 and day 500 in the SSH coordinate. Particle density peaks at -0.06 m and -0.2 m SSH level at day 400, and at -0.06 m and -0.22 m at day 500 (Fig. 11). The bi-modal distribution is a robust feature that appears both in the SOSE simulation, and also in the DIMES US2 tracer measurements and in other numerical simulations (LaCasce et al. 2014; Tulloch et al. 2014).

Around day 800, when more than 80% of the particles have entered DP (Figure 13), the maximum of the particle PDF jumps from -0.25 m to about -0.5 m. This resembles the leaky jets regime discussed by Thompson and Sallée (2012) and by Naveira Garabato et al. (2011). Fronts often act as barriers to cross-frontal tracer transport. However, fronts tend to break and meander over the topographic transition regions leading to enhanced cross-frontal transport. This enhancement is further illustrated in the bifurcations in particle trajectories shown in Figure 12. Here groups of particles start from the same location but reach different latitudes and SSH levels. The blue and yellow lines represent the particles that went eastward toward the Scotia Arc. These particles clearly drift away from the rest only after passing the Shackleton Ridge (blue) and Endurance Fracture Zone (yellow) (Figure 12). The majority of the particles (purple, green, red) in the SAF and PF travel northward over the North Scotia Ridge near 49°W, 53.3°S, and then diverge into three main pathways. One branch (red) follows the south rim of the Falkland Plateau. It first travels eastward and then northward toward Falkland Fracture Zone near 38°W, 49°S. The two other branches (green and purple) travel over the Falkland Plateau. One overshoots at the Falkland Escarpment toward the Argentine abyssal plane and then travels eastward (green). Another (purple) follows the continental slope within the Malvinas Current and eastward after reaching the Brazil-Malvinas confluence zone. The original small tracer patch is distributed over a broad range of latitudes and SSH levels due to these trajectory bifurcations. The bifurcations are a result of the topographic break-down of the jet inhibition of cross-frontal transport, denoted as the "leaky jet effect".

To summarize, particle PDF evolution shows enhanced cross-stream transport as particles passing through regions with strong topographic influence, i.e., the DP and Scotia Sea longitude. The enhanced cross-stream exchange is consistent with the *leaky* jet argument. In theory, strong geostrophic fronts inhibit cross-frontal tracer transport due to potential vorticity constraints. In an idealized flat bottom periodic channel configuration, mixing is enhanced only near the critical layer, where the propagation speed of a perturbation is equal and opposite to the speed of the mean flow (e.g., Ferrari and Nikurashin 2010). In reality, ACC fronts vary substantially along stream resulting from interactions with bottom topography. The strong topographic regulation results in an enhanced cross-stream exchange associated with jet breaking points (Thompson and Sallée 2012; Naveira Garabato et al. 2011; Sallée et al. 2011). In these leaky jet regions, cross-stream exchange is also enhanced due to the originally tightly-packed streamlines (Abernathey and Cessi 2014). Four major topographic features that are associated with enhanced cross-frontal transport are the Shackleton Ridge, fracture zones in the Scotia Sea, the North Scotia Ridge and the Falkland Plateau. The DP and Scotia Sea regions function as a blender generating vigorous cross-frontal transport.

d. *The vertical distribution of the cross frontal transport*

The simulated point tracer release shows that the particles that originate at 110°W on the 27.9 neutral density layer between the SAF and the PF in the southeast Pacific drift poleward. This is consistent with the zonally averaged SOMOC, in which the poleward and upward upwelling branch is sandwiched between the 27.6 and 28.0 neutral density layers. Now we extend this to analyze a full latitude-depth section. Particles are released along a latitude-depth section from 70°S to 45°S and from top to bottom at 110°W. The particles originate from a mesh with 1/12° meridional grid spacing and 10-m vertical spacing, and are advected for 5 years in SOSE.

In Lagrangian coordinates, the time-mean cross-stream transport is simply the difference between particle coordinates at the end and the beginning of an averaging period:

$$\Delta\psi \mid_{t_1}^{t_2} = \psi(t_2|x_0, y_0, z_0, t_0) - \psi(t_1|x_0, y_0, z_0, t_0).$$

The $\Delta\psi$ is a true Lagrangian integration, and accounts for both mean and eddy effects. With a sufficiently long averaging time, it becomes less sensitive to inaccuracies in the choice of streamline coordinate.

We subdivide the first 1000 days into two 500-day periods. Particles mostly stay in the southeast Pacific region during the first 500 days and then pass through DP during the second 500 days. Figure 14 shows $\Delta\psi \mid_{0d}^{500d} (y_0, z_0)$ and $\Delta\psi \mid_{500d}^{1000d} (y_0, z_0)$ at the particle release coordinates. We overlay the 27.6 and 28.0 neutral density contours, because they bound the poleward upwelling branch in the zonally averaged Southern Ocean meridional overturning circulation (Lumpkin and Speer 2007; Mazloff et al. 2013).

During the first 500 days, the cross-stream transport shown by particles (top panel of Figure 14) indicates that particles move both northward and southward relative to the reference streamlines, with no clear SOMOC structure. Changes in SSH are of large amplitude, due to the fact that the ACC fronts in the deep southeast Pacific are not anchored by topography so that the time-mean SSH does not act as a guide for particles. The displacement data indicate no clear difference in dynamics in the upper ocean compared with the deeper ocean in the southeast Pacific.

During the second 500 days, most of the particles have gone through DP, and especially those released above the 28.0 level. In the lower panel of Figure 14, the well-organized band of the poleward particle transport clearly corresponds to the poleward-upwelling region between 27.6 and 28.0. Above and below the poleward band, particles tend to move equatorward. This banded structure implies the presence of a well-defined meridional overturning circulation within a zonally averaged framework. The fact that the meridional overturning is not detectable in the first 500 days suggests that the zonally-averaged SOMOC is governed by processes that occur in DP and in the regions to its east. The poleward-upwelling in the SOMOC is a result of the imbalance between wind-driven northward Ekman transport and isopycnal relaxation by mesoscale eddies. Ekman transport tends to lift isopycnals to increase the local baroclinicity, but mesoscale eddies act opposing effect. Thompson and Naveira Garabato (2014) noted that the isopycnal slope is steeper upstream than downstream of major topographic features. The downstream smaller isopycnal slope is due to enhanced baroclinic instability associated with topography (MacCready and Rhines 2001). Our diagnosis indicates that Circumpolar Deep Water is carried southward across sreamlines primarily in the hot spots associated with topography.

While local cross-stream exchanges could appear to be amplified if time-mean streamlines have less curvature than instantaneous streamlines, the long-term average shows a clear subsurface poleward transport sandwiched between the 27.6 and 28.0 neutral density layers, corresponding to the Upper Circumpolar Deep Water and to the poleward transport in the SOMOC. The MOC-like pattern of the subsurface poleward transport forms after the particles enter DP, highlighting the importance of local dynamics in contributing to zonally averaged quantification. This regional contrast echoes earlier studies (e.g., Thompson and

Sallée 2012) that estimated that local hot-spots of cross frontal exchange occupy only 20% of the ACC zonal extent but can account for more than 75% of the total cross-frontal exchange.

5. Conclusions

This study has validated the SOSE particle dispersion against the DIMES tracer measurements. One million particles are used to represent the 76 kg CF_3SF_5 released by DIMES and advected by the SOSE velocity fields. The direct comparisons show that SOSE is effective in simulating the DIMES measurements, both in terms of the horizontal spreading and in terms of the cross-stream transport.

Sensitivity studies based on SOSE particles show that the Lagrangian sub-grid mixing parameterization on particles is important for a point-tracer simulation. A random walk model with K_h = 20-30 m^2 s^{-1} is optimal for the particle simulation in the 1/6 degree SOSE. This scaling is consistent with Boland et al. (2015) who used DIMES tracer measurements to infer that the submesoscale mixing in the southeast Pacific is about 25 m^2 s^{-1}.

The sensitivity studies also show that the initial dynamical condition is an important factor for realistic simulation of the tracer spreading during the first two years. DIMES tracer was released in a stagnant region of the southeast Pacific, and advected westward during the first month. This initial westward transport influenced the timing of downstream spreading. Without the initial stall, tracers travel faster in model simulations than in observations. The SOSE simulation with particles released in a similar stagnant region near the DIMES tracer release location match the DIMES measurements better than the simulation with particles released exactly at the DIMES tracer release location but with a different dynamical condition.

Both SOSE particles and the DIMES tracer show a robust poleward transport of the tracer. For the SOSE simulation, this transport is associated with several localized hot-spots for cross-stream transport, including the Shackleton Ridge, the fracture zones in the

Scotia Sea, the north Scotia Ridge, and the Falkland Plateau. The enhanced cross-frontal transport in these regions, especially in the Drake Passage and Scotia Sea regions, is due to the "leaky jet effect" associated with topographic influence. Particles travel within jets and are easily leaked out at topographic transition regions where jets often break into eddies and streamlines begin to diverge. Streamlines first converge before entering the DP, then diverge at the exit. This geometric configuration, formed by bathymetry, also facilitates the cross-stream transport.

We also carry out a particle release experiment initializing on a depth-latitude section along 110°W to study the local MOC. The results show that the upwelling branch of the zonally-averaged SOMOC between the 27.6 and 28.0 neutral density levels is clearly represented by the particle shift in streamline coordinate. The particle SSH shift shows a pattern that resembles the zonally averaged SOMOC, but only after particles pass through the DP and Scotia Sea regions, thus demonstrating the importance of these regions in forming the Southern Ocean meridional circulation. This is consistent with theories in which eddy fluxes are enhanced downstream of elevated topography due to increased baroclinic instability. The DP and Scotia Sea longitudes are hot-spots for the poleward along-isopycnal transport of the Southern Ocean Circumpolar Deep Waters. It is hypothesized that the poleward-upwelling in the zonally-averaged SOMOC is accomplished by a limited number of hot-spots. Here we focused on the DP regions; a detailed decomposition of the zonally-averaged SOMOC in a Lagrangian framework for the rest of the Southern Ocean is left for future work.

Acknowledgments.

The DIMES experiment is supported by the Natural Environment Research Council (NERC) of the U.K. and U.S. National Science Foundation. We also thank the scientists, crew and technicians on the RRS James Cook, the RRS James Clark Ross, and the R/V Thomas G. Thompson. Wang, Mazloff and Gille are supported by NSF OCE-1234473 and PLR-1425989. Messias is supported by NERC NE/E005985/2, Watson is supported by

The Royal Society, and Ledwell is supported by NSF OCE7232962. The offline Lagrangian particle tracking model (Octopus) is open source with The MIT License and available at https://github.com/jinbow/Octopus.

APPENDIX A

Particle-Tracer Projection

There are three sources of errors in Lagrangian tracer simulations. The first one comes from the discretization of a continuous distribution of fluid into a finite number of particles. This type of error is related to Lagrangian resolution, which in principle is similar to the resolution in Eulerian models. The discretization error can be reduced by increasing the number of particles.

The second type of error comes from the Eulerian velocity field. In our Lagrangian particle tracking model, particle motions are not constrained to obey Newtonian laws, i.e., particles are regarded as massless and have no acceleration nor interaction. Instead, particle velocities are obtained from a companion Eulerian model. Particles can move within an Eulerian grid box, but their velocities are derived from an interpolation of the Eulerian velocity. First of all, the degree of the realism of the Eulerian model, which suffers from a lack of spatial resolution, is often low. Errors inherited from the less realistic Eulerian model can not be reduced by any amendment to the Lagrangian method. In this study, the SOSE fields are chosen, as they have been proven in previous studies to be consistent with most observations. Second, the interpolation process can introduce uncertainties in long-range trajectories. These uncertainties can be reduced by ensemble average.

The third type of error comes from the mapping of discrete particles onto a mesh to retrieve tracer concentration. There are many weighting functions W for the mapping (Bagtzoglou et al. 1992). The most direct way is the box-counting method, which divides the total volume into grid boxes and measures tracer concentration as the enclosed particle mass divided by the grid volume δV in three dimensions, or the grid area δA in two dimensions.

The 2D box-counting weighting function W is written as

$$W(\mathbf{x}-\mathbf{x}_i(t)) = \begin{cases} \frac{1}{\delta x \delta y} & |x-x_i| \le \delta x;\ |y-y_i| \le \delta y \\ 0 & \text{elsewhere.} \end{cases}$$

This method is computationally efficient for a regular grid, but becomes difficult to apply for irregular ones. In addition, one needs a large number of particles to realistically represent a true tracer field especially after the initial point-tracer widely spreads.

There are other smooth weighting functions that consider particle mass to be spatially structured instead of a delta function. It is equivalent to consider the weighting function as a probability distribution of the particle position. Assuming that the probability distribution is Gaussian, the weighting function is

$$W(\mathbf{x}-\mathbf{x}_i(t)) = \frac{1}{\delta x \delta y} \exp\left(-\frac{\pi(x-x_i(t))^2}{\delta x^2} - \frac{\pi(y-y_i(t))^2}{\delta y^2}\right).$$

In principle, a large number of particles and smoother weighting functions are associated with smaller mapping error. Here we test the dependence of the mapping error on the number of particles N and the width of the weighting function δx or δy. We conduct the test based on a one-dimensional tracer profile, assuming the tracer distribution isotropic. A tracer field with a Gaussian concentration distribution,

$$\hat{C}(x) = \frac{1}{\sqrt{2\pi}} \exp\left(-\frac{x^2}{2}\right),$$

can be represented by a cloud of N particles with a normal distribution

$$x_i = \mathcal{N}(0,1),\ i = 0 \cdots N-1, \tag{A1}$$

where $\mathcal{N}(0,1)$ represents the normal distribution with zero mean and unit variance. The total tracer mass is $\int_{-\infty}^{\infty} \hat{C} \mathrm{d}x = 1$, and the particle mass is $c = 1/N$. Substituting these relations into Eq. A1, we get the tracer concentration. The tracer concentration is evaluated on a grid consisting of N_g bins within $-5 < x < 5$. The resulting mapped tracer concentration has resolution $\delta x = 10/N_g$. The mapping error ϵ is defined as

$$\epsilon = r.m.s\left(C(n\delta x) - \hat{C}(n\delta x)\right),\ n = 1 \cdots N_g.$$

Figure 15 shows the noise to signal ratio $\epsilon\sqrt{2\pi}$ of (a) the box-counting and (b) the Gaussian methods as a function of N_g and N. The Gaussian method always outperforms the box-counting method especially over the small N_g and large N range (see Figure 15c). For a small number of particles (<1000), smaller N_g results in smaller error. The larger error associated with the smaller N_g is due to over-smoothing. In general, mapping errors decrease as the number of particles N increases. Figure (16) shows the error as a function of number of particles per grid box taken along $N_g = 100$. The mapping error is proportional to $N^{-1/2}$ for both methods, which is consistent with previous studies (Bagtzoglou et al. 1992).

Mapping error increases with time too, because as a tracer blob expands due to diffusion, the number of particles per grid box will decrease, resulting in increased mapping error. For a pure diffusive process, the size of a tracer blob scales as $L_{tracer} \sim (2\mathbf{K}t)^{1/2}$, where $\mathbf{K}$ is the diffusivity. Consequently, the number of particles per grid box decreases as a function of $(2\mathbf{K}t)^{-1/2}$ given a fixed number of particles. The mapping errors then increase as a function of $(2\mathbf{K}t)^{1/2}$. Combining two error sources together gives

$$\epsilon \sim \left(\frac{2\mathbf{K}t}{N}\right)^{1/2}.$$

This relationship is for an infinite domain, where the tracer blob can expand indefinitely. However, for an enclosed domain such as an ocean basin with length scale L, there exists an upper bound on $\epsilon_{bound} \sim L/N^{1/2}$, because particles are not spreading forever. The timescale for reaching ϵ_{bound} is $t_{bound} = L^2/\mathbf{K}$, in which the relationship $L_{tracer} = (2\mathbf{K}t)^{1/2}$ is used.

These relationships can be used to infer the optimal number of particles needed for a certain simulation. For example, by requiring each grid box with size Δx to contain the optimal number of particles N_{optm}, the optimal number of particles scales as

$$N \geq 4\pi\mathbf{K}tN_{optm}/\Delta x^2, \tag{A2}$$

where $4\pi\mathbf{K}t$ corresponds to the area of a tracer blob at time t with the diffusivity of the turbulent field $\mathbf{K}$, and $4\pi\mathbf{K}tN_{optm}/\Delta x^2$ corresponds to the number of grid box within the tracer blob at time t with Δx being the Eulerian tracer resolution. Take the scaling in the southeast Pacific region, substituting $\mathbf{K} \sim 700$ m^2 /s (Tulloch et al. 2014), $t = 500$ days, $\Delta x \sim 20$ km to Eq. A2, then the optimal number of particles is

$$N \approx 38000.$$

This is a back-of-envelop calculation. We further tested this relationship using the one million particles. Figure 17 shows the percentage of the variance as a function of particle numbers at the end of 500 days. We found that 35000 particles are sufficient to represent 98% of the variance of the one million particles. One caveat is that we derived the relation based only on diffusive physics. This relation can be slightly difference for cases concerning intermittent turbulent patches and for cases with strong shears.

APPENDIX B

Lagrangian particle tracking

Particle tracking

We integrate particle trajectories using the deterministic SOSE velocities and a parameterized diffusion process. The deterministic part from SOSE is

$$\frac{d\mathbf{x}_i}{dt} = \mathbf{v}_i,$$

where $\mathbf{x}_i$ is the position of the i_{th} particle and $\mathbf{v}_i$ is its interpolated SOSE velocity vector. The sub-grid parameterized process is simulated by a Lagrangian stochastic process. SOSE implements a constant horizontal hyper-diffusivity and hyper-viscosity and vertical Laplacian diffusivity and viscosity. There is no direct way of representing the hyper-diffusivity using particles, so we scale the hyper-diffusivity to a Laplacian diffusivity. The tracer concentration tendency due to a Laplacian diffusion is $\frac{\partial C}{\partial t} = \nabla \cdot \mathbf{K}\nabla C$, where $\mathbf{K}$ represents the diffusivity vector $(\kappa_x, \kappa_y, \kappa_z)$. This down-gradient effective diffusion is meant to represent the mixing due to the Brownian motion and can be modeled by a random walk scheme in a Lagrangian model. There is then an additional displacement for each particle due to sub-grid turbulence

$$\Delta\mathbf{x}_i = \sqrt{2\mathbf{K}\delta t}\,\omega(t), \tag{B1}$$

where ω represents a Weiner process of unit variance and δt denotes the time step for the particle trajectory integration. The particle trajectory in a discrete form becomes

$$\mathbf{x}_i^{n+1} = \mathbf{x}_i^n + \mathbf{v}_i\delta t + \sqrt{2\mathbf{K}\delta t}\,\omega(t),$$

where n represents the number of time step. The evolution of the second moment of a cloud of particles follows

$$\frac{d\langle \mathbf{x} - \overline{\mathbf{x}}\rangle^2}{dt} = 2\mathbf{K}, \tag{B2}$$

where $\langle\cdot\rangle$ represents the ensemble average and $\overline{\mathbf{x}}$ represents the center of mass. In practice, the random number generator for ω should be carefully chosen because not all are suitable for use in random walk models (Hunter et al. 1993). Here we implement the normal random number generator algorithm described by Kinderman and Monahan (1977). The second moment of a cloud of particles simulated by the generator follows Eq. (B2) within one standard deviation (figure not shown).

Mixed layer parameterization

The nonlocal K-profile parameterization (KPP) (Large et al. 1994) is used in SOSE to represent the unresolved processes involved in vertical mixing in the surface mixed-layer. KPP encapsulates the turbulent mixing generated by shear instability and convection into a simple parameterized flux form

$$\overline{wx}(d) = -K\left(\frac{\partial X}{\partial z} - \gamma\right), \tag{B3}$$

where $\overline{wx}$ represents the turbulent vertical flux, K represents the parameterized boundary layer vertical diffusivity, $\partial X/\partial z$ is the vertical gradient of a mean property X (momentum, active and passive tracers), and γ represents a non-local transport invoked by convection (Large et al. 1994). The boundary layer diffusivity K is a function of depth and specified as $K(\sigma) = hw(\sigma)G(\sigma)$, where $\sigma = d/h$ is a dimensionless vertical coordinate that varies from 0 to 1 in the boundary layer with a height of h and $G(\sigma)$ is a non-dimensional vertical shape function.

The particle behavior corresponding to the KPP parameterization is more complicated to simulate than the case with constant background eddy diffusivities. As K is z-dependent, we should consider the effect of the spatial variation of K in the evolution of the tracer distribution. Define the normalized n-th moment of a tracer C as $N_n^* = M_n/M_0$, where

$M_n = \int_{-\infty}^{\infty} Cx^n \mathrm{d}x$. It can be shown that

$$\frac{d}{dt}N_1^* = K' \tag{B4}$$

$$\frac{d}{dr}N_2^* = 2K(0) + 4K'N_1^* \tag{B5}$$

where $K(0)$ is the zeroth order Taylor expansion of K, and K' represents $\mathrm{d}K/\mathrm{d}z$ (Hunter et al. 1993). With the proper initial condition that sets $N_1^* = N_2^* = 0$ at $t = 0$, the first and second moments are proportional to $N_1^* = K't$ and $N_2^* = 2K(N_1^*)t$, respectively. This means that with the presence of a slowly varying diffusivity, the center of mass represented by N_1^* drifts with a velocity K' toward regions with larger diffusivities. The second moment relative to the origin increases similarly to the constant diffusivity case but with K evaluated at the location of the center of mass, which is changing with time. The discretized particle trajectory associated with the spatially slowly varying diffusivity is

$$z_i^{n+1} = z_i^n + (w_i + K'(z_i^n))\delta t + \sqrt{2K(z_i^n + K'(z_i^n)\delta t)\delta t}\,\omega(t) \tag{B6}$$

The nonlocal transport flux $K\gamma$ can be modeled by a particle-reshuffling process within mixed layer as described in the next section.

Offline calculation

Our goal is to develop an efficient method for studies that require a large number of ensembles with a large number of particles. The particle module included in the MITgcm packages enables the model to calculate online particle trajectories (Klocker and Ferrari 2012). However, the online particle tracking becomes unaffordable when the number of ensemble becomes large. We aim to test an efficient offline particle tracking method using the available SOSE output.

The particle tracking model retrieves particle velocity using tri-linear interpolation scheme in space and linear interpolation in time from the surrounding 8 gridded SOSE velocity points at two successive time steps. The model uses an explicit fourth-order Runge-Kutta scheme for trajectory integration. The model implements the reflective boundary condition at the surface and bottom. The reflective boundary condition is important in correctly simulating tracers especially near the bottom of small valleys.

The SOSE horizontal hyper-diffusivity is scaled to a Laplacian diffusivity and parameterized using a random walk module. The particle behavior can become much more complicated for mixed-layer processes. The ideal case is a direct simulation of the KPP process, with depth-dependent K profile and a non-local transport, as described in the previous section. The offline computation of mixed-layer processes, however, is limited by the time interval of the model output, δt^{output} hereafter, which is longer than the time interval required by the direct simulation as described below.

The time step, Δt, for accurate particle track integration is upper-bounded by several factors related to the dominant length, velocity, grid size, and time scales. First, Δt should be smaller than the eddy time scale to avoid aliasing in the temporal domain and to capture the correct eddy variability. The dominant time scale for the Southern Ocean eddy variability is more than order of 10 days (figure not shown). Second, we need $\Delta t < L_e/U_e$, where L_e and U_e are the eddy length and velocity scales, respectively, to ensure that particles will well sample and not jump through eddies within one time step. Consider $L_e \sim 50$ km and $U_e \sim 20$ cm/s, then $\Delta t < 2.9$ days. Third, the "equivalent diffusive velocity" is $U_d = \sqrt{2K/\Delta t}$ given a diffusivity coefficient K. We require Δt to be small enough to ensure that the spreading of a tracer patch will not exceed, within one time step, the eddy length L_e or the typical domain size for example the mixed-layer depth so that $L_e > U_d \Delta t$. Given a horizontal diffusivity $K = 800$ m^2/s and an eddy length scale $L_e \sim 50$ km, $\Delta t < L_e^2/2K \equiv 18$ days. Within the mixed-layer, the KPP diffusivity K_{kpp} can become as large as 2×10^{-2} m^2/s. Assuming mixed-layer depth $h_{mld} \sim 50$ m, we get $\Delta t < h_{mld}^2/K_{kpp} \equiv 1.5$ days.

Based on the above scaling, using 1-day-averaged velocity in the Iteration 100 is sufficient to represent the mesoscale eddy activities. We approximate the particle behavior in the mixed-layer using a random displacement model with a uniform distribution in the vertical direction,

$$z_i^{n+1} = (h_{mld} + \Delta h) R(0,1), \text{ if } z_i^n < h_{mld}, \tag{B7}$$

where Δh represents the thickness of the transition layer through which water can be advected into and out of the mixed-layer, and $R(0,1)$ represents the uniform distribution with the lower bound 0 and upper bound 1. We assume that the surface mixed-layer will be well-mixed within a limit of days, so that mixed-layer particles are "shuffled" every five days in our model.

The daily-averaged output also captures the high frequency energy energy between 1 and 5 days. The high-frequency eddy energy is relatively small in the ACC core regions but not in the regions near islands and shallow sea mounts or outside the ACC core (Fig. 18), where the high-frequency energy is probably due to fast barotropic or coastal trapped waves.

REFERENCES

Abernathey, R. and P. Cessi, 2014: Topographic enhancement of eddy efficiency in baroclinic equilibration. *J. Phys. Oceanogr.*, 140507124027009, doi:10.1175/JPO-D-14-0014.1.

Abernathey, R., J. Marshall, and D. Ferreira, 2011: The dependence of Southern Ocean meridional overturning on wind stress. *J. Phys. Oceanogr.*, **41 (12)**, 2261–2278, doi:10.1175/JPO-D-11-023.1.

Bagtzoglou, A. C., A. F. B. Tompson, and D. E. Dougherty, 1992: Projection functions for particle-grid methods. *Numer. Methods Partial Differ. Equ.*, **8 (4)**, 325–340, doi:10.1002/num.1690080403.

Belkin, I. M. and A. L. Gordon, 1996: Southern Ocean fronts from the Greenwich meridian to Tasmania. *J. Geophys. Res.*, **101 (C2)**, 3675–3696, doi:10.1029/95JC02750.

Boland, E. J. D., E. Shuckburgh, P. H. Haynes, J. R. Ledwell, M.-J. Messias, and A. J. Watson, 2015: Estimating a sub-mesoscale diffusivity using a roughness measure applied to a tracer release experiment in the Southern Ocean. *J. Phys. Oceanogr.*, 150406094850002, doi:10.1175/JPO-D-14-0047.1.

Chapman, C. C., 2014: Southern Ocean jets and how to find them: Improving and comparing common jet detection methods. *J. Geophys. Res. Ocean.*, **119**, 4318–4339, doi:10.1002/2014JC009810.

Cunningham, S. and M. Pavic, 2007: Surface geostrophic currents across the Antarctic circumpolar current in Drake Passage from 1992 to 2004. *Prog. Oceanogr.*, **73 (3-4)**, 296–310, doi:10.1016/j.pocean.2006.07.010.

Döös, K., V. Rupolo, and L. Brodeau, 2011: Dispersion of surface drifters and model-simulated trajectories. *Ocean Model.*, **39 (3-4)**, 301–310, doi:10.1016/j.ocemod.2011.05.005.

Ducet, N., P. Y. Le Traon, and G. Reverdin, 2000: Global high-resolution mapping of ocean circulation from TOPEX/Poseidon and ERS-1 and -2. *J. Geophys. Res.*, **105 (C8)**, 19 477–19 498.

Dufour, C. O., et al., 2015: Role of mesoscale eddies in cross-frontal transport of heat and biogeochemical tracers in the Southern Ocean. *J. Phys. Oceanogr.*, submitted.

Ferrari, R. and M. Nikurashin, 2010: Suppression of eddy diffusivity across jets in the Southern Ocean. *J. Phys. Oceanogr.*, **40 (7)**, 1501–1519, doi:10.1175/2010JPO4278.1.

Firing, Y. L., T. K. Chereskin, and M. R. Mazloff, 2011: Vertical structure and transport of the Antarctic Circumpolar Current in Drake Passage from direct velocity observations. *J. Geophys. Res.*, **116 (C8)**, C08 015, doi:10.1029/2011JC006999.

Forget, G., 2010: Mapping ocean observations in a dynamical framework: A 2004–06 ocean atlas. *Journal of Physical Oceanography*, **40 (6)**, 1201–1221, doi:10.1175/2009JPO4043.1.

Gille, S. T., 1994: Mean sea surface height of the Antarctic Circumpolar Current from Geosat data: Method and application. *J. Geophys. Res.*, **99 (C9)**, 18 255, doi:10.1029/94JC01172.

Gille, S. T., 1997: The Southern Ocean momentum balance: Evidence for topographic effects from numerical model output and altimeter data. *J. Phys. Oceanogr.*, **27 (10)**, 2219–2232.

Gille, S. T., 2012: Diurnal variability of upper ocean temperatures from microwave satellite measurements and Argo profiles. *J. Geophys. Res.*, **117 (C11)**, C11 027, doi:10.1029/2012JC007883.

Gille, S. T., 2014: Meridional displacement of the Antarctic Circumpolar Current. *Philos. Trans. A. Math. Phys. Eng. Sci.*, **372 (2019)**, 20130 273, doi:10.1098/rsta.2013.0273.

Gille, S. T., K. Speer, J. R. Ledwell, and A. C. Naveira Garabato, 2007: Mixing and stirring in the Southern Ocean. *Eos, Trans. Am. Geophys. Union*, **88**, 382, doi: 10.1029/2007EO390002.

Griesel, A., S. T. Gille, J. Sprintall, J. L. McClean, J. H. LaCasce, and M. E. Maltrud, 2010: Isopycnal diffusivities in the Antarctic Circumpolar Current inferred from Lagrangian floats in an eddying model. *J. Geophys. Res.*, **115 (C6)**, C06 006, doi: 10.1029/2009JC005821.

Griesel, A., M. R. Mazloff, and S. T. Gille, 2012: Mean dynamic topography in the Southern Ocean: Evaluating Antarctic Circumpolar Current transport. *J. Geophys. Res.*, **117 (C1)**, C01 020, doi:10.1029/2011JC007573.

Griffies, S. M., 2004: *Fundamentals of Ocean Climate Models*. Princeton University Press, 556 pp.

Hallberg, R. and A. Gnanadesikan, 2006: The role of eddies in determining the structure and response of the wind-driven Southern Hemisphere overturning: Results from the Modeling Eddies in the Southern Ocean (MESO) Project. *J. Phys. Oceanogr.*, **36 (12)**, 2232–2252, doi:10.1175/JPO2980.1.

Hughes, C. W. and E. R. Ash, 2001: Eddy forcing of the mean flow in the Southern Ocean. *J. Geophys. Res.*, **106 (C2)**, 2713, doi:10.1029/2000JC900332.

Hunter, J., P. Craig, and H. Phillips, 1993: On the use of random walk models with spatially variable diffusivity. *J. Comput. Phys.*, **106**, 366–376.

Johnson, G. C. and H. L. Bryden, 1989: On the size of the Antarctic Circumpolar Current. *Deep Sea Res. Part A. Oceanogr. Res. Pap.*, **36 (1)**, 39–53, doi:10.1016/0198-0149(89)90017-4.

Kinderman, A. and J. Monahan, 1977: Computer generation of random variables using the ratio of uniform deviates. *ACM Trans. Math. Softw.*, **3 (3)**, 257–260.

Klocker, A. and R. Ferrari, 2012: Reconciling float-based and tracer-based estimates of lateral diffusivities. *J. Mar. Res.*, **70 (4)**, 569–602, doi:10.1357/002224012805262743.

LaCasce, J. H., R. Ferrari, J. Marshall, R. Tulloch, D. Balwada, and K. Speer, 2014: Float-derived isopycnal diffusivities in the DIMES experiment. *J. Phys. Oceanogr.*, **44 (2)**, 764–780, doi:10.1175/JPO-D-13-0175.1.

Large, W. G., J. C. Mcwilliams, and S. C. Doney, 1994: Oceanic vertical mixing: a review and a model with a nonlocal boundary layer parameterization. *Rev. Geophys.*, **32 (4)**, 363–403.

Ledwell, J. R., L. C. St. Laurent, J. B. Girton, and J. M. Toole, 2011: Diapycnal mixing in the Antarctic Circumpolar Current. *J. Phys. Oceanogr.*, **41 (1)**, 241–246, doi:10.1175/2010JPO4557.1.

Liu, Y., A. MacFadyen, Z.-G. Ji, and R. H. Weisberg, (Eds.) , 2011: *Monitoring and Modeling the Deepwater Horizon Oil Spill: A Record-Breaking Enterprise*, Geophysical Monograph Series, Vol. 195. American Geophysical Union, Washington, D. C., doi:10.1029/GM195.

Lumpkin, R. and K. Speer, 2007: Global ocean meridional overturning. *J. Phys. Oceanogr.*, **37 (10)**, 2550–2562, doi:10.1175/JPO3130.1.

MacCready, P. and P. B. Rhines, 2001: Meridional transport across a zonal channel: Topographic localization. *J. Phys. Oceanogr.*, **31 (6)**, 1427–1439, doi:10.1175/1520-0485(2001)031⟨1427:MTAAZC⟩2.0.CO;2.

Mariano, A. J., V. Kourafalou, A. Srinivasan, H. Kang, G. Halliwell, E. Ryan, and M. Roffer, 2011: On the modeling of the 2010 Gulf of Mexico Oil Spill. *Dyn. Atmos. Ocean.*, **52 (1-2)**, 322–340, doi:10.1016/j.dynatmoce.2011.06.001.

Marshall, J. and T. Radko, 2003: Residual-mean solutions for the Antarctic Circumpolar Current and its associated overturning circulation. *J. Phys. Oceanogr.*, **33 (11)**, 2341–2354, doi:10.1175/1520-0485(2003)033⟨2341:RSFTAC⟩2.0.CO;2.

Marshall, J. and K. Speer, 2012: Closure of the meridional overturning circulation through Southern Ocean upwelling. *Nat. Geosci.*, **5 (3)**, 171–180, doi:10.1038/ngeo1391.

Mazloff, M. R., R. Ferrari, and T. Schneider, 2013: The force balance of the Southern Ocean Meridional Overturning Circulation. *J. Phys. Oceanogr.*, **43 (6)**, 1193–1208, doi:10.1175/JPO-D-12-069.1.

Mazloff, M. R., P. Heimbach, and C. Wunsch, 2010: An eddy-permitting Southern Ocean state estimate. *J. Phys. Oceanogr.*, **40 (5)**, 880–899, doi:10.1175/2009JPO4236.1.

Messias, M., et al., 2015: Hotspots of deep-ocean mixing in the Antarctic Circumpolar Current from a tracer perspective. *Science (80-.)*., submitted.

Monaghan, J., 1992: Smoothed particle hydrodynamics. *Annu. Rev. Astron. Astrophys*, **30**, 543–74.

Munk, W. and E. Palmen, 1951: Note on the dynamics of the Antarctic Circumpolar Current. *Tellus*, **3 (1)**, 53–55, doi:10.1111/j.2153-3490.1951.tb00776.x.

Naveira Garabato, A. C., R. Ferrari, and K. L. Polzin, 2011: Eddy stirring in the Southern Ocean. *J. Geophys. Res. Ocean.*, **116 (9)**, doi:10.1029/2010JC006818.

Naveira Garabato, A. C., D. P. Stevens, A. J. Watson, and W. Roether, 2007: Short-circuiting of the overturning circulation in the Antarctic Circumpolar Current. *Nature*, **447 (May)**, 194–197, doi:10.1038/nature05832.

Orsi, A. H., T. Whitworth, and W. D. Nowlin, 1995: On the meridional extent and fronts of the Antarctic Circumpolar Current. *Deep Sea Res. Part I Oceanogr. Res. Pap.*, **42 (5)**, 641–673, doi:10.1016/0967-0637(95)00021-W.

Pavlis, N. K., S. a. Holmes, S. C. Kenyon, and J. K. Factor, 2012: The development and evaluation of the Earth Gravitational Model 2008 (EGM2008). *J. Geophys. Res.*, **117 (B4)**, B04 406, doi:10.1029/2011JB008916.

Peña Molino, B., S. R. Rintoul, and M. R. Mazloff, 2014: Barotropic and baroclinic contributions to along-stream and across-stream transport in the Antarctic Circumpolar Current. *J. Geophys. Res. Ocean.*, **119 (11)**, 8011–8028, doi:10.1002/2014JC010020.

Sallée, J., K. Speer, and S. Rintoul, 2011: Mean-flow and topographic control on surface eddy-mixing in the Southern Ocean. *J. Mar. Res.*, **69 (4)**, 753–777, doi:10.1357/002224011799849408.

Sallée, J. B., K. Speer, R. Morrow, and R. Lumpkin, 2008: An estimate of Lagrangian eddy statistics and diffusion in the mixed layer of the Southern Ocean. *J. Mar. Res.*, **66 (4)**, 441–463, doi:10.1357/002224008787157458.

Sallée, J.-B., K. Speer, S. Rintoul, and S. Wijffels, 2010: Southern Ocean thermocline ventilation. *J. Phys. Oceanogr.*, **40 (3)**, 509–529, doi:10.1175/2009JPO4291.1.

Sheen, K. L., et al., 2013: Rates and mechanisms of turbulent dissipation and mixing in the Southern Ocean: Results from the Diapycnal and Isopycnal Mixing Experiment in the Southern Ocean (DIMES). *J. Geophys. Res. Ocean.*, **118**, doi:10.1002/jgrc.20217.

Sokolov, S. and S. R. Rintoul, 2002: Structure of Southern Ocean fronts at 140 °E. *J. Mar. Syst.*, **37 (1-3)**, 151–184, doi:10.1016/S0924-7963(02)00200-2.

Sokolov, S. and S. R. Rintoul, 2007: Multiple jets of the Antarctic Circumpolar Current south of Australia. *J. Phys. Oceanogr.*, **37 (5)**, 1394–1412, doi:10.1175/JPO3111.1.

Sokolov, S. and S. R. Rintoul, 2009: Circumpolar structure and distribution of the Antarctic Circumpolar Current fronts: 1. Mean circumpolar paths. *J. Geophys. Res.*, **114 (C11)**, C11 018, doi:10.1029/2008JC005108.

St. Laurent, L., A. C. Naveira Garabato, J. R. Ledwell, A. M. Thurnherr, J. M. Toole, and A. J. Watson, 2012: Turbulence and diapycnal mixing in Drake Passage. *J. Phys. Oceanogr.*, **42 (12)**, 2143–2152, doi:10.1175/JPO-D-12-027.1.

Stohl, A., C. Forster, A. Frank, P. Seibert, and G. Wotawa, 2005: Technical note: The Lagrangian particle dispersion model FLEXPART version 6.2. *Atmos. Chem. Phys.*, **5 (9)**, 2461–2474, doi:10.5194/acp-5-2461-2005.

Terada, H. and M. Chino, 2008: Development of an atmospheric dispersion model for accidental discharge of radionuclides with the function of simultaneous prediction for multiple domains and its evaluation by application to the Chernobyl nuclear accident. *J. Nucl. Sci. Technol.*, **45 (9)**, 920–931, doi:10.1080/18811248.2008.9711493.

Thompson, A. F., P. H. Haynes, C. Wilson, and K. J. Richards, 2010: Rapid Southern Ocean front transitions in an eddy-resolving ocean GCM. *Geophys. Res. Lett.*, **37 (23)**, L23 602, doi:10.1029/2010GL045386.

Thompson, A. F. and A. C. Naveira Garabato, 2014: Equilibration of the Antarctic Circumpolar Current by standing meanders. *J. Phys. Oceanogr.*, **44 (7)**, 1811–1828, doi:10.1175/JPO-D-13-0163.1.

Thompson, A. F. and J.-B. Sallée, 2012: Jets and topography: Jet transitions and the impact on transport in the Antarctic Circumpolar Current. *J. Phys. Oceanogr.*, **42 (6)**, 956–972, doi:10.1175/JPO-D-11-0135.1.

Tulloch, R., et al., 2014: Direct estimate of lateral eddy diffusivity upstream of Drake Passage. *J. Phys. Oceanogr.*, **44 (10)**, 2593–2616, doi:10.1175/JPO-D-13-0120.1.

van Sebille, E., M. H. England, J. D. Zika, and B. M. Sloyan, 2012: Tasman leakage in a fine-resolution ocean model. *Geophys. Res. Lett.*, **39**, doi:10.1029/2012GL051004.

van Sebille, E., P. Spence, M. R. Mazloff, M. H. England, S. R. Rintoul, and O. A. Saenko, 2013: Abyssal connections of Antarctic Bottom Water in a Southern Ocean State Estimate. *Geophys. Res. Lett.*, **40 (10)**, 2177–2182, doi:10.1002/grl.50483.

van Sebille, E., P. J. van Leeuwen, A. Biastoch, C. Barron, and W. P. M. de Ruijter, 2009: Lagrangian validation of numerical drifter trajectories using drifting buoys: Application to the Agulhas system. *Ocean Model.*, **29 (4)**, 269–276, doi:10.1016/j.ocemod.2009.05.005.

Watson, A. J., J. R. Ledwell, M.-J. Messias, B. a. King, N. Mackay, M. P. Meredith, B. Mills, and A. C. Naveira Garabato, 2013: Rapid cross-density ocean mixing at mid-depths in the Drake Passage measured by tracer release. *Nature*, **501 (7467)**, 408–11, doi:10.1038/nature12432.

Weijer, W., M. E. Maltrud, W. B. Homoky, K. L. Polzin, and L. R. M. Maas, 2015: Eddy-driven sediment transport in the Argentine Basin: Is the height of the Zapiola Rise hydrodynamically controlled? *J. Geophys. Res. Ocean.*, **120 (3)**, 2096–2111, doi:10.1002/2014JC010573.

List of Tables

TABLE 1. The timing information of the eight DIMES cruises.

Cruise	Time	days since US1
US1	(1/8/2009-2/24/2009)	–
US2	(1/16/2010-3/1/2010)	344
UK2	(12/1/2010-1/20/2011)	663
UK2.5	(4/9/2011-4/26/2011)	792
US3	(8/20/2011-8/20/2011)	925
UK3	(1/31/2012-3/22/2012)	1089
UK4	(3/9/2013-5/1/2013)	1492
UK5	(3/9/2014-3/24/2014)	1857

List of Figures

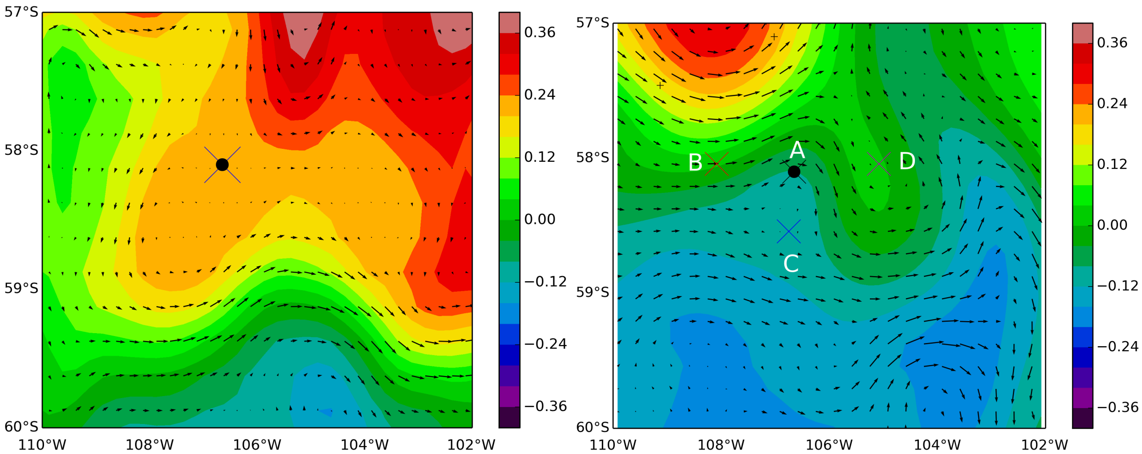

FIG. 1. The SSH fields with the local mean removed (contours) for DIMES US1 (left) and SOSE particle simulations (right). The SSH fields are the February 3, 2009 snapshot from the AVISO product (left), and the February 5, 2005 from SOSE (right). The vectors represent the surface geostrophic velocity derived from the SSH. In the right panel, the vectors represent the velocity field at 1550 meters. The black dot-cross symbols in both panels mark the same DIMES tracer release location. The B, C, and D mark the locations of the three other tracer release tested in the particle simulations. The distances to the DIMES location A, are 85 km, 50 km, and 92 km for B, C, and D, respectively. All locations are between the SAF and PF.

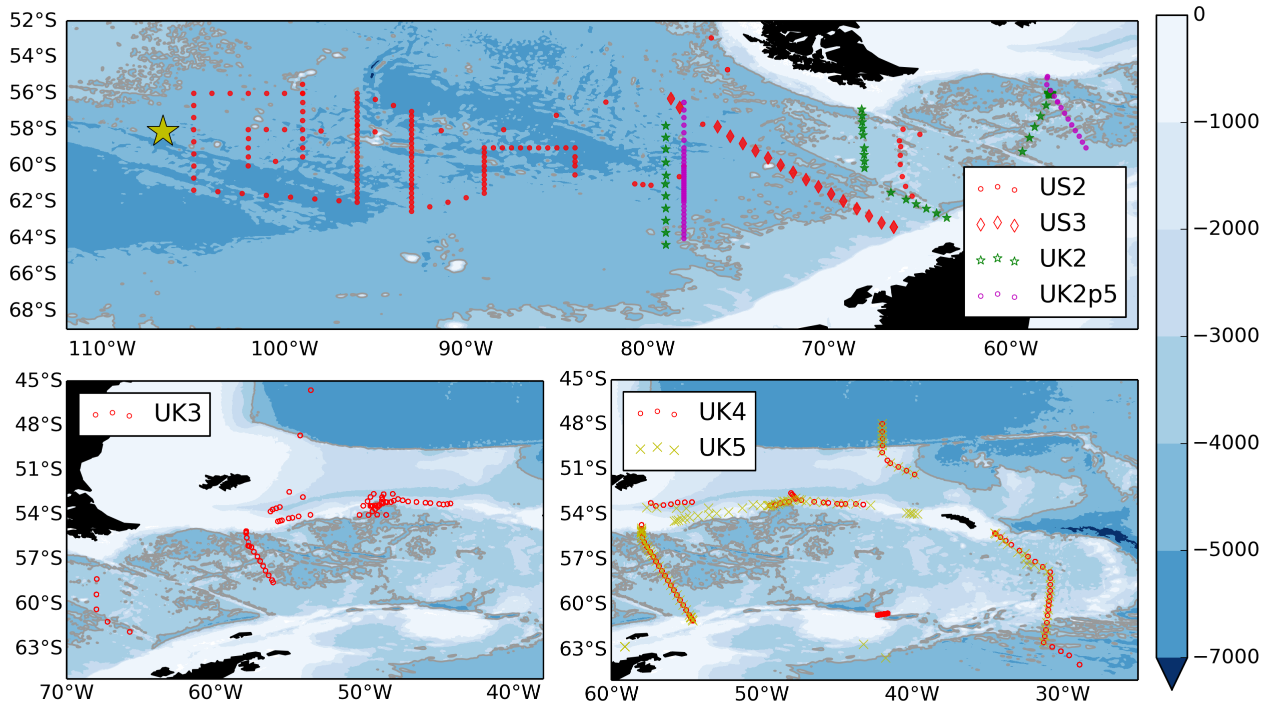

FIG. 2. The location of DIMES CTD stations superimposed on a colored bathymetry map. The gray contour marks the 4000-meter isobath.

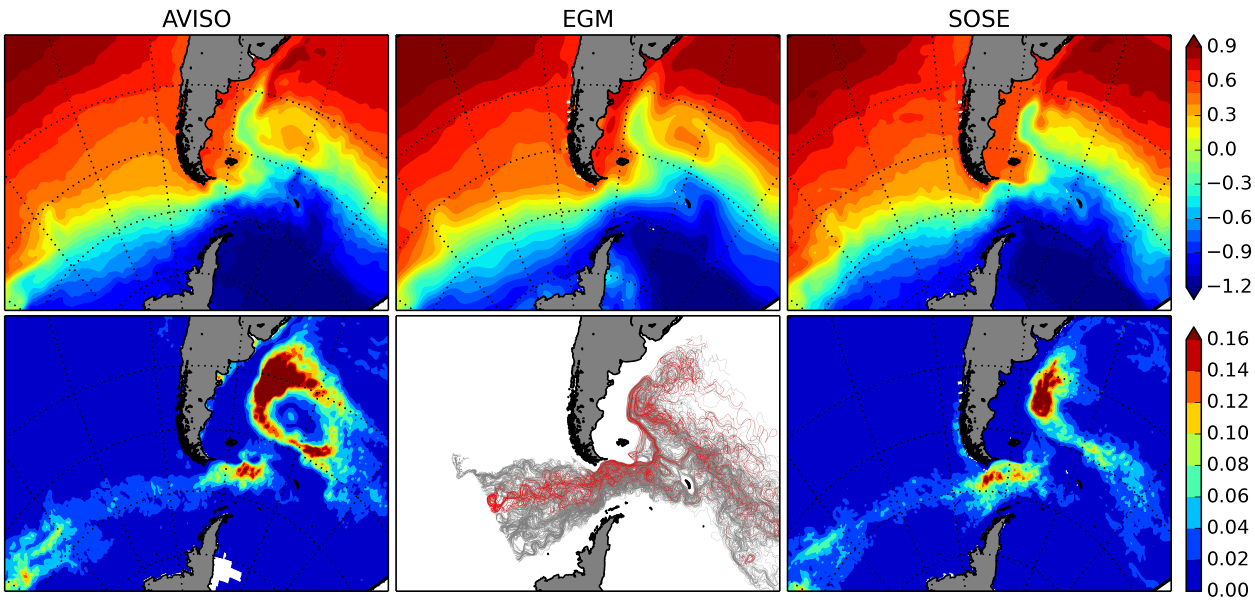

FIG. 3. Top: comparison of the 6-year-mean SSH between the SOSE (right) and the satellite products (AVISO on the left and EGM08 in the top middle). The AVISO eddy kinetic energy (EKE) is shown in bottom left panel, and SOSE EKE in bottom right panel. The bottom-middle panel shows a subsample of the particles trajectories (grey) released along 106.7°W. Red trajectories represent particles released near the DIMES tracer release location.

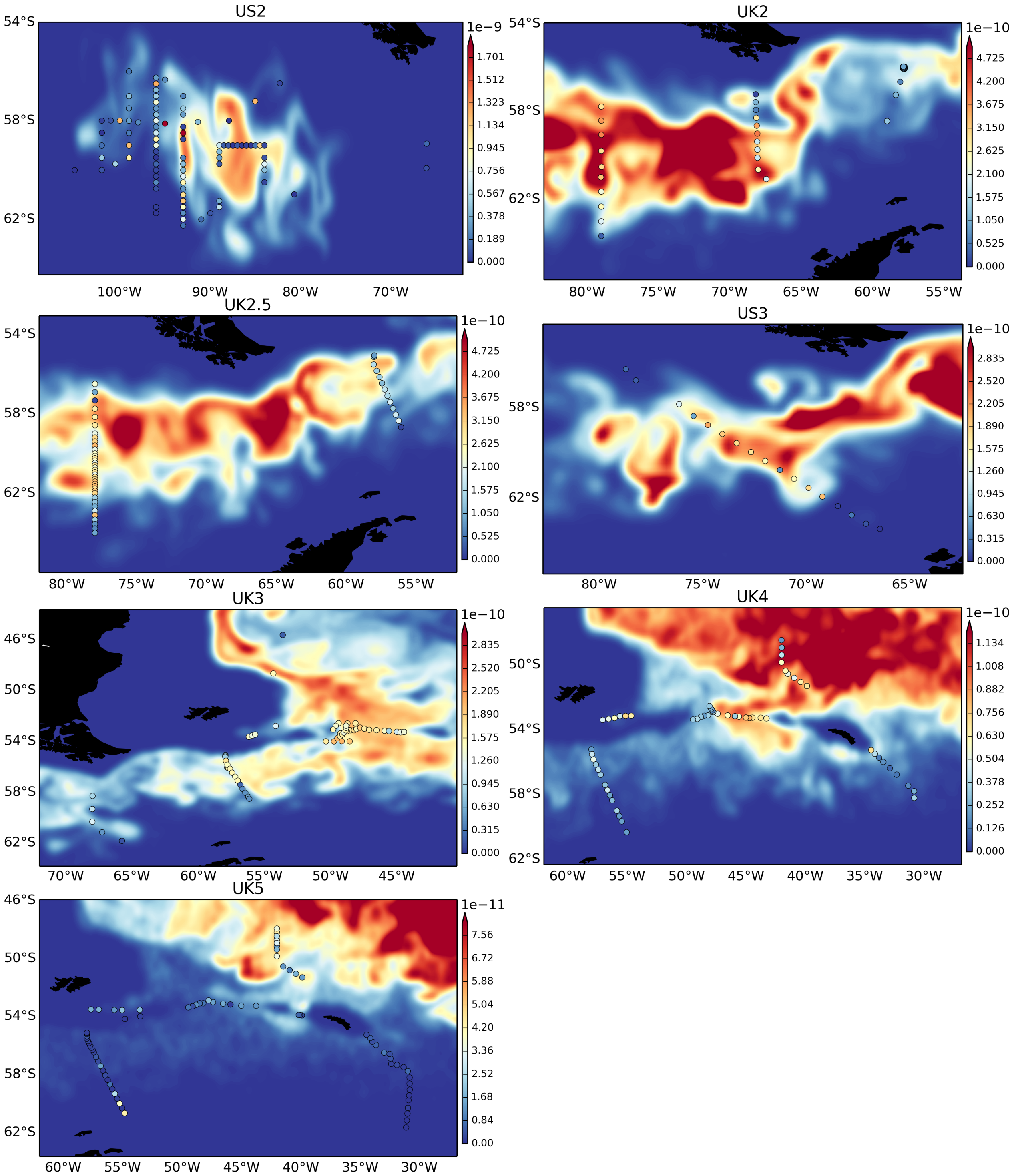

FIG. 4. The column integrated tracer concentration (mole/m^2) location of DIMES CTD stations. The color contours are for the model and the circles are for the station locations, with the same color scale for both.

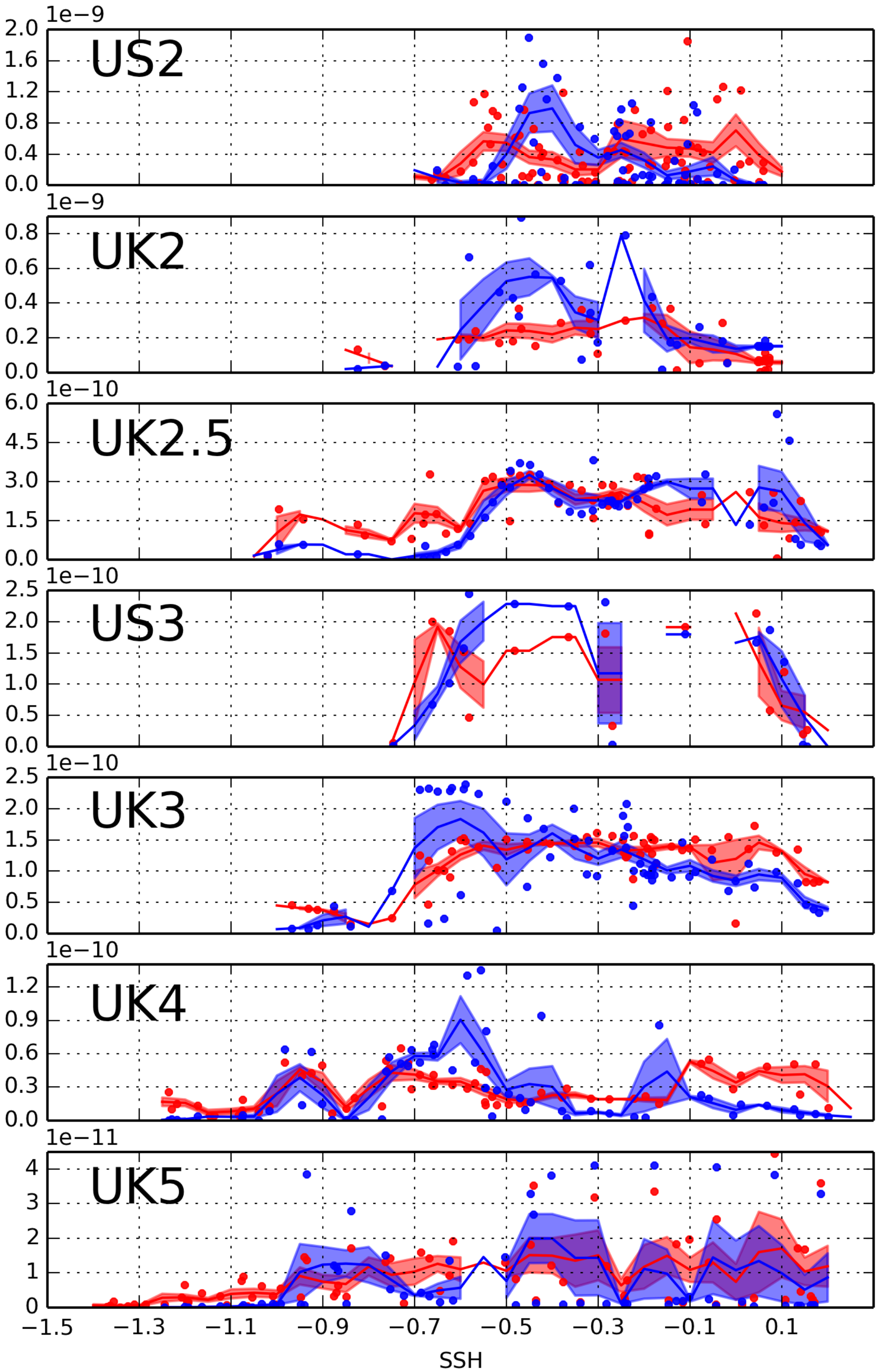

FIG. 5. The tracer concentration plotted in the SSH coordinate. Each dot represents one tracer measurement. Red dots represent DIMES measurements and blue ones represent the sample of SOSE simulation interpolated to the same DIMES CTD locations. The lines represent the mean of the tracer concentration in the 0.05m-wide SSH bins. The colored envelopes indicate the standard error for the points in each bin. The standard error is not plotted for bins with fewer than 3 samples.

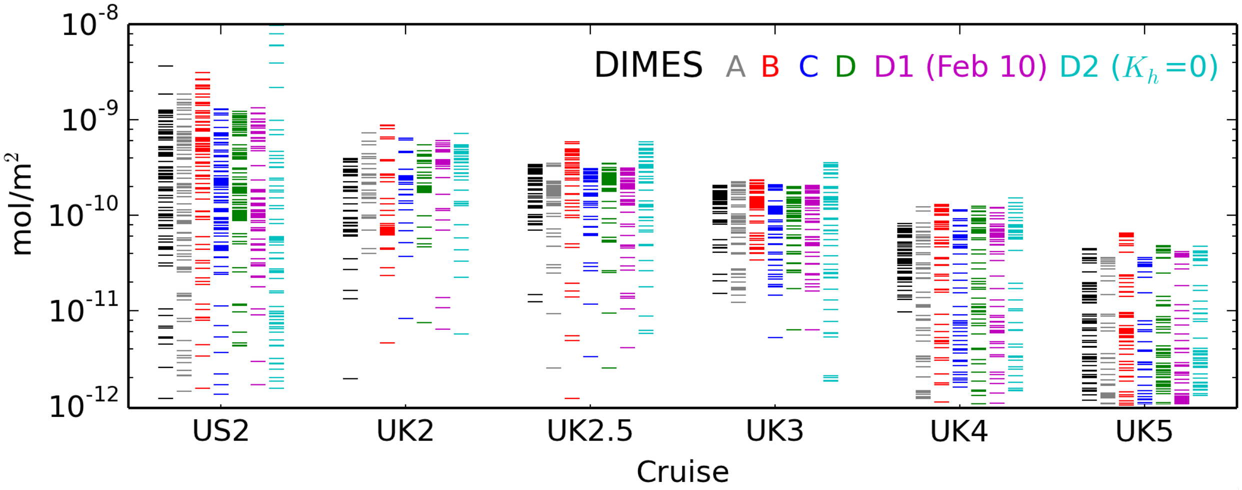

Fig. 6. The direct comparison of the DIMES tracer measurements (black) with the SOSE tracer simulations (color). The case A (gray), B (red), C (blue), D (green) represent the simulations with the particles released on February 1, 2005 at location A, B, C, D marked in Figure (1), respectively. The case D1 (magenta) has the initial particles released on February 10, 2005. K_h=25 m^2/s in all case but D2 (cyan), where K_h=0 m^2/s is used.

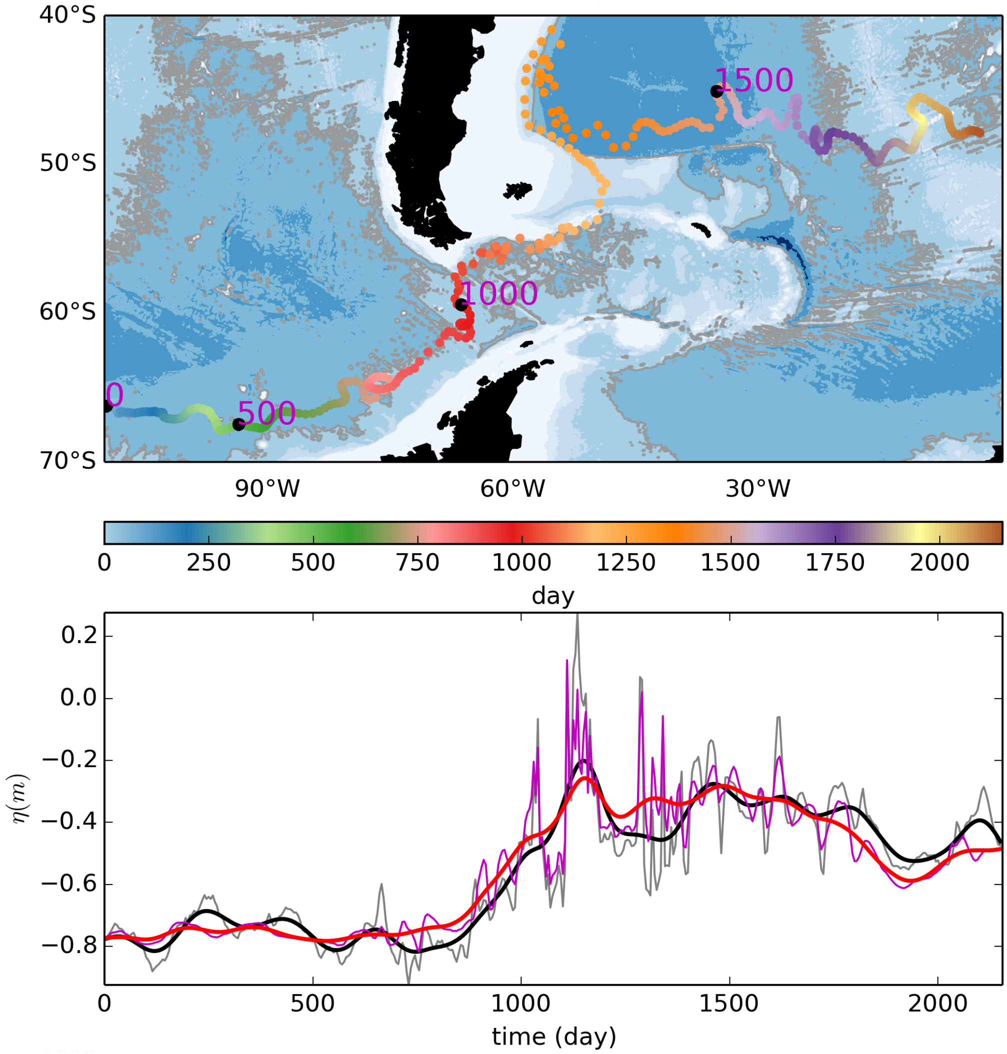

FIG. 7. A randomly chosen particle trajectory (top) color-coded with time lapsed from the release. The particle SSHs as a function of time (bottom). The 60-day averaged and 6-year averaged SSHs recorded along the trajectory are shown in gray and purple, respectively. The thick black (red) line represents the 200-day smoothing mean of the gray (purple) line.

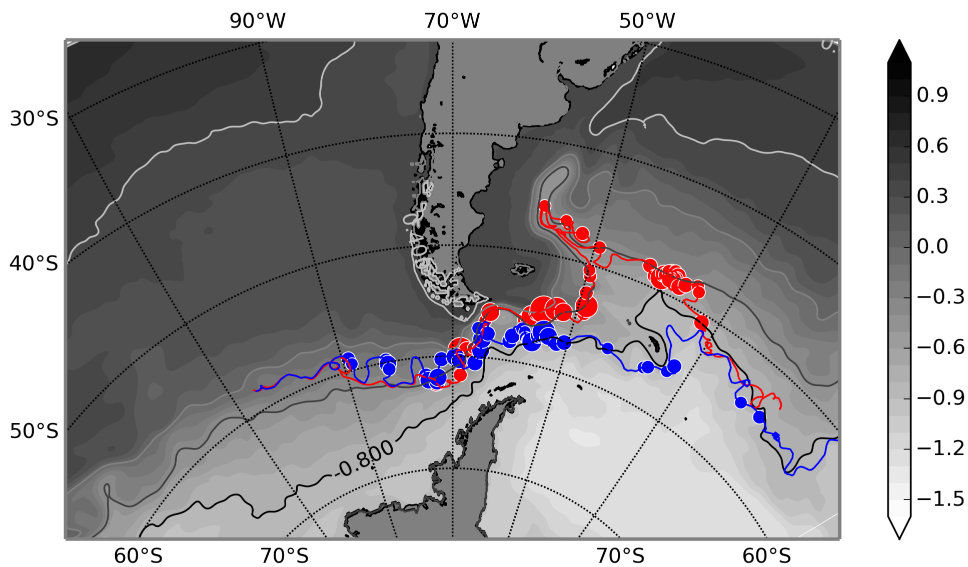

Fig. 8. An example of two particle trajectories. The colored dots represent the location and amplitude of the cross-streamline events. The time mean SSH field is show by the background contours.

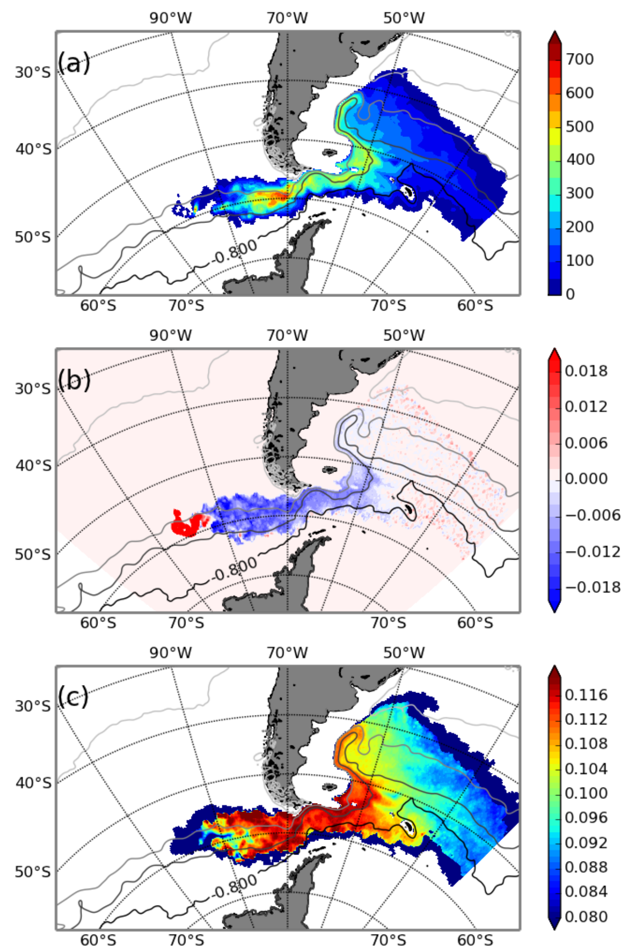

FIG. 9. The ensemble average of the frequency of (a) the cross-frontal exchange and (b) the mean and (c) the mean of the absolute $d\psi/5days$.

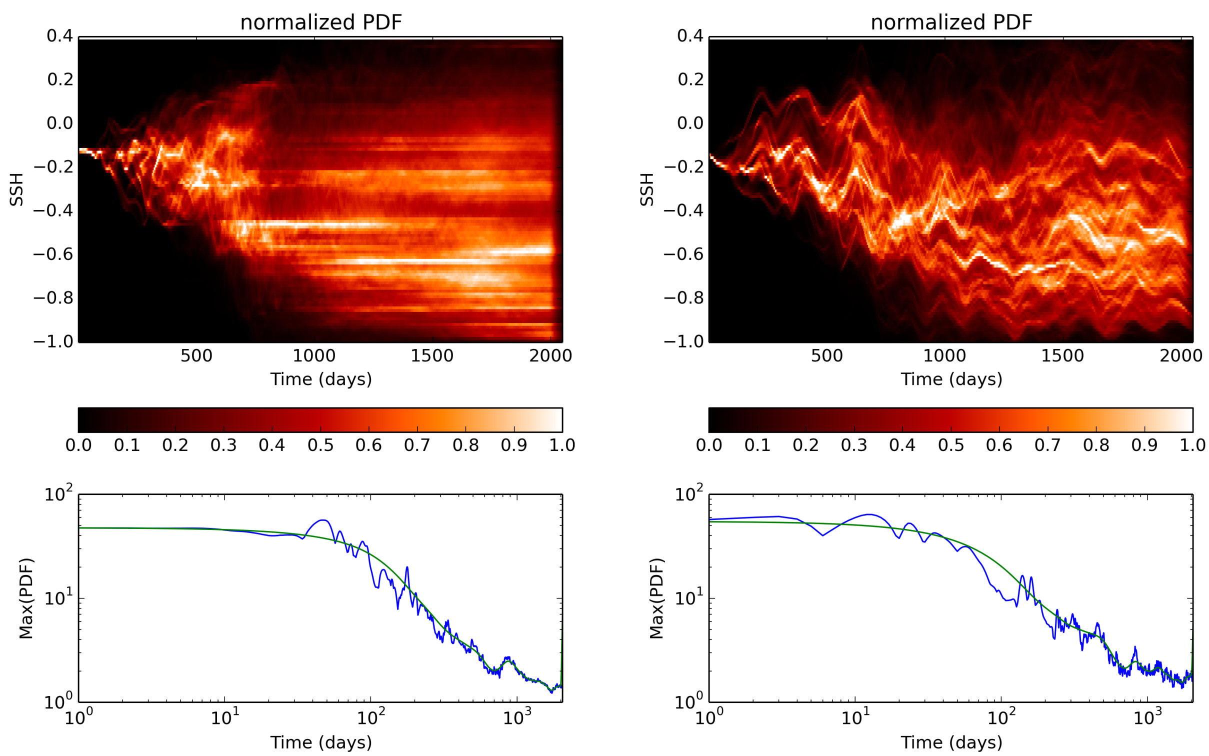

FIG. 10. Upper: the Hovmöller diagram of the normalized particle probability density function in SSH coordinates. It is normalized with respect to the maximum value at each time step shown in the lower panel. The maximum in the PDF at each time step is shown in blue and the 200-day running mean is shown in green. The left (right) panel shows results based on 6-year mean (60-day running mean) SSH.

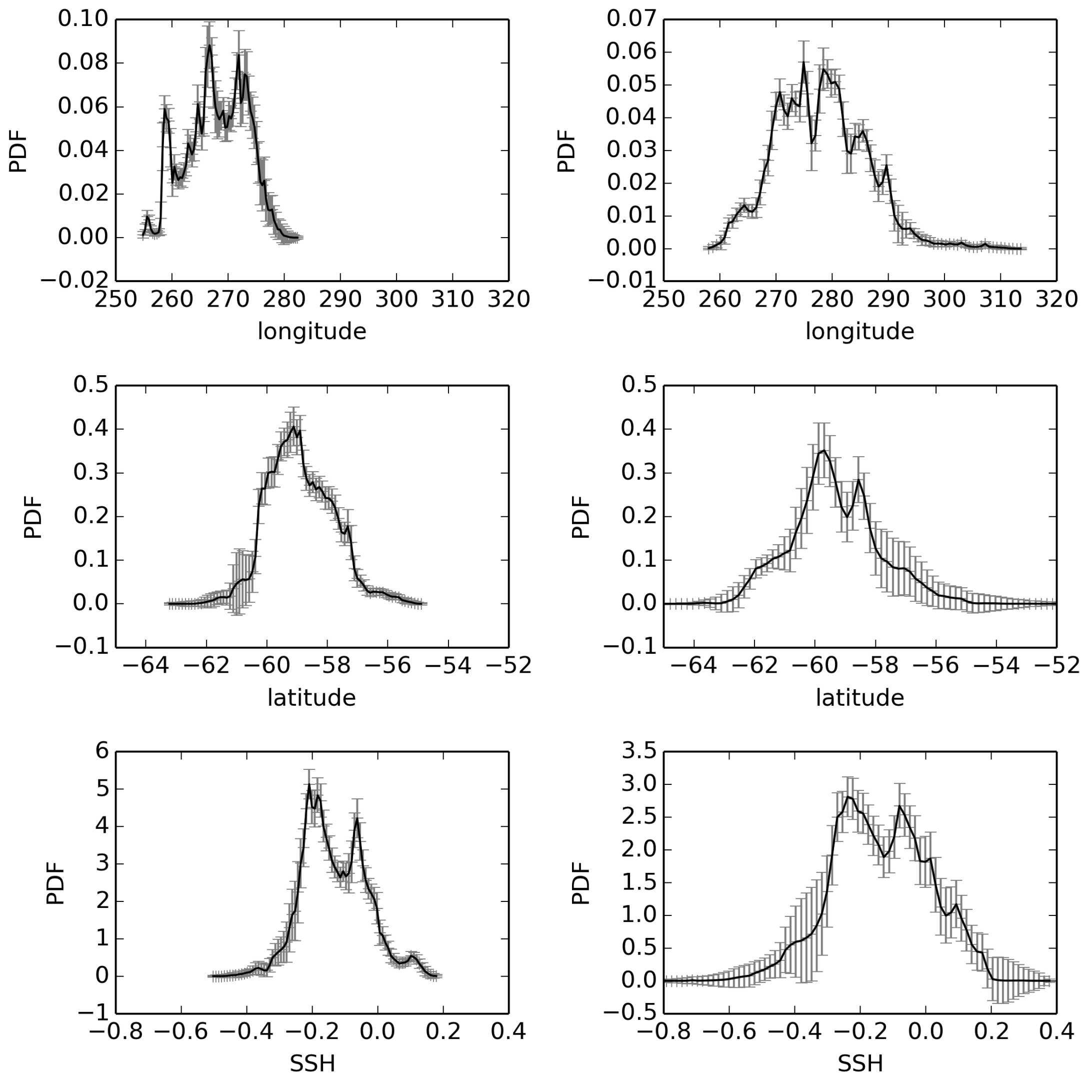

Fig. 11. The particle PDF in longitude (top), latitude (middle) and SSH (bottom) coordinate at 400 (left) and 500 (right) days. Uncertainties shown by errorbars are estimated by bootstrapping 1000 times of subsamples consisting 5000 particles.

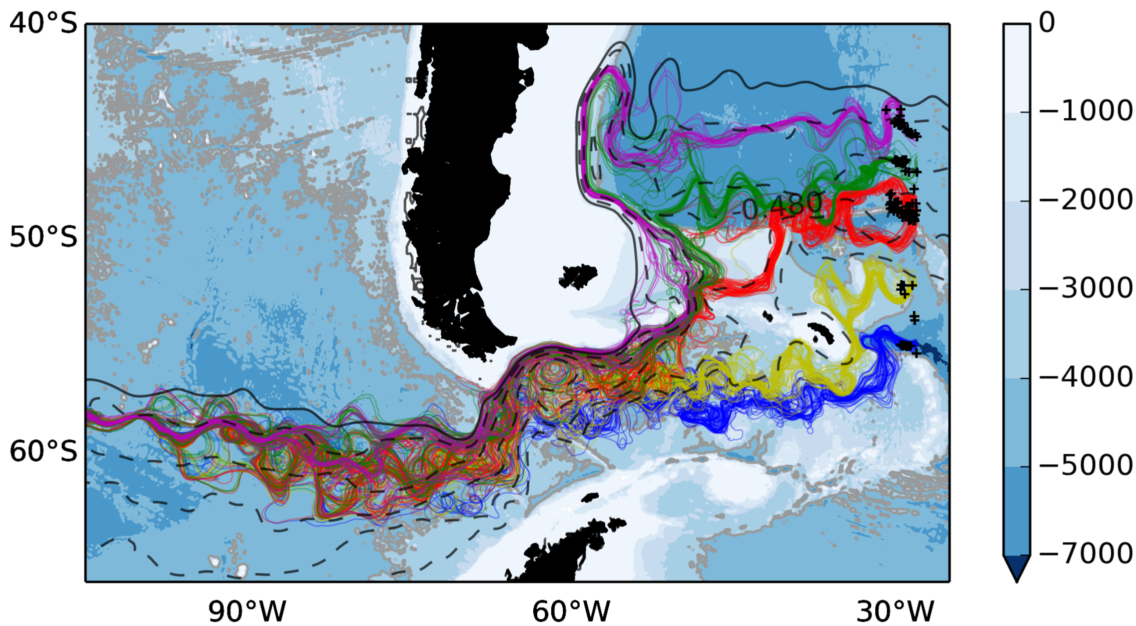

Fig. 12. The particle trajectories that went through different latitude by day 1100. Each group has 60 lines color-coded by the latitude band through which they passed cross 31°W at 1100 days. The blue background shows bathymetry derived from ETOPO1. The black contours show the mean SSH field.

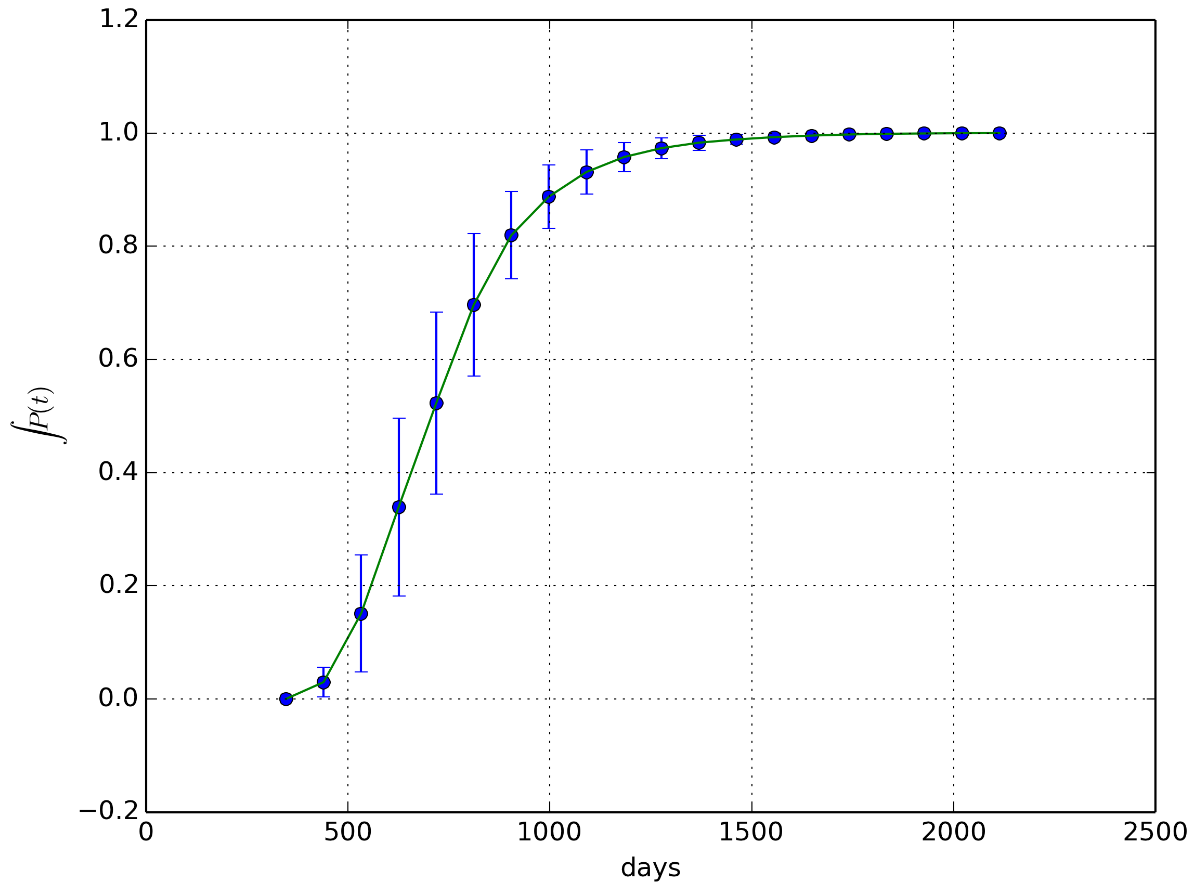

FIG. 13. The cumulative probability function of particle reaching the DP entrance, defined at 68.25°W, after certain days (x-axis).

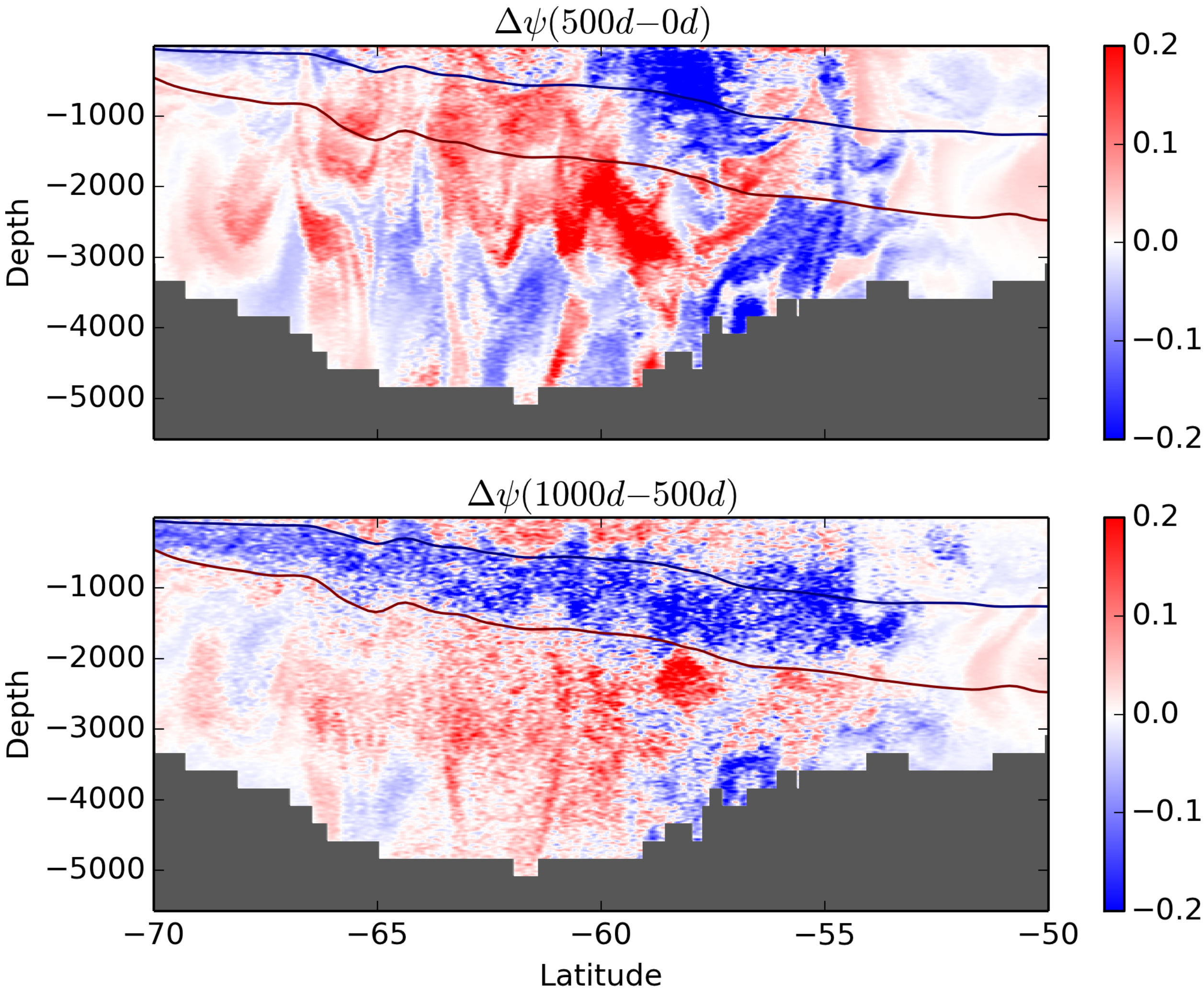

FIG. 14. The cross-stream transport $\Delta\psi$ averaged between the first 500 days (top) and the second 500 days (bottom) projected back to the depth section at 110∘W. The 27.6 and 28.0 neutral density levels along the particle release longitude, 110W, is superimposed. The two neutral density levels are conventionally used as the boundaries enclosing the upwelling branch of the Upper Circumpolar Deep Water (Lumpkin and Speer 2007).

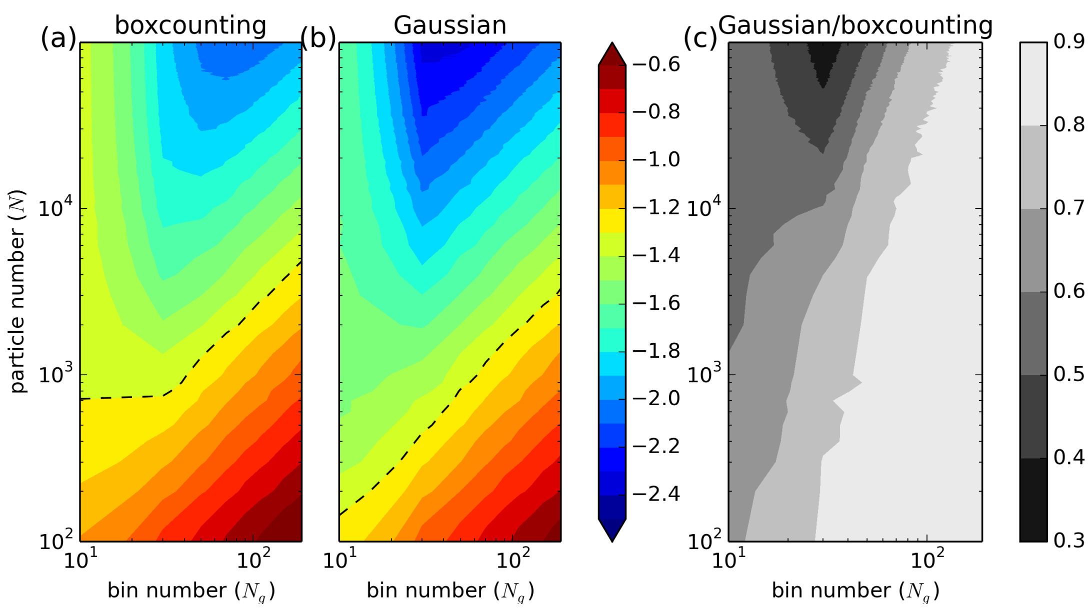

FIG. 15. The ensemble-averaged (200 realizations) standard error σ on $\log_{10}$ scale between the true tracer concentration $\hat{C}$ in Eq. (5) and the reconstructed tracer concentration based on particles for (a) the box-counting method and (b) the Gaussian weighting method. (c) The ratio of errors between the box-counting and Gaussian methods, $\sigma_{boxcounting}/\sigma_{Gaussian}$.

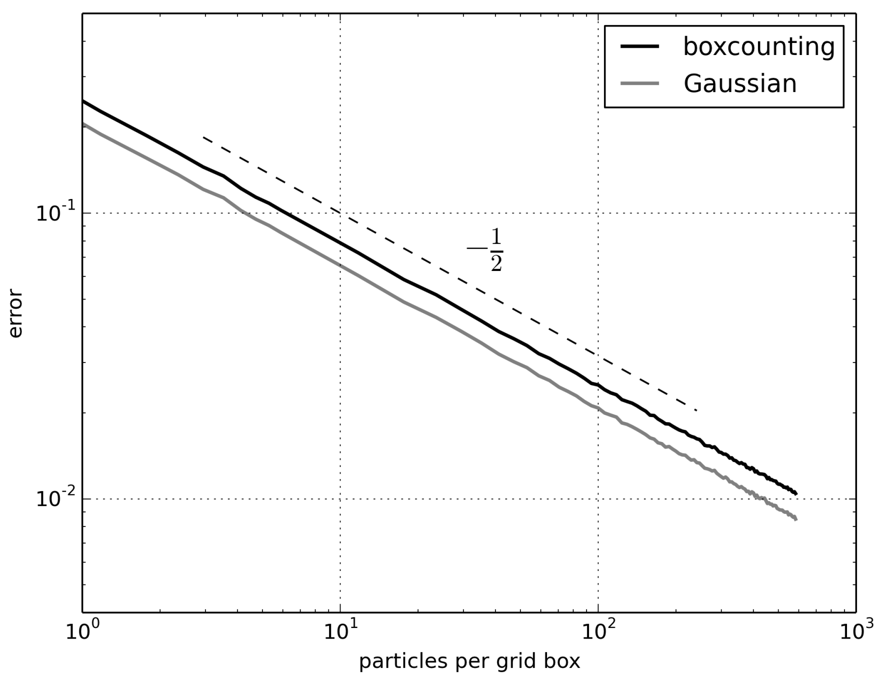

FIG. 16. Error estimate based on a one-dimensional Gaussian. The black line shows the result of the boxcounting method, and the gray line of the Gaussian method.

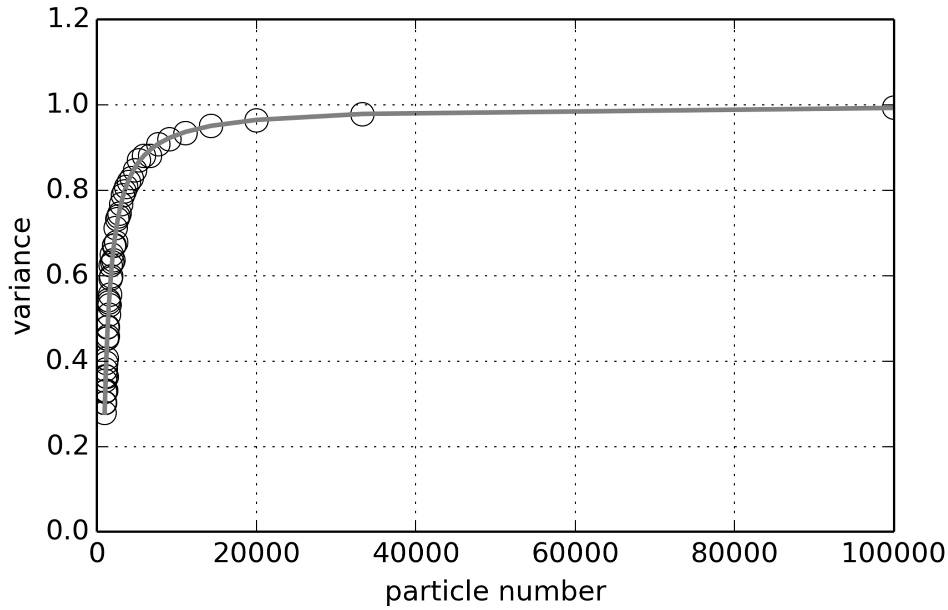

FIG. 17. The percentage of variance of the tracer patch mapped from one million particles at the end of 500 days as a function of number of particles, which are randomly sampled out of the one million ones. The circles represent direct numerical calculation. The grey line represents analytical prediction.

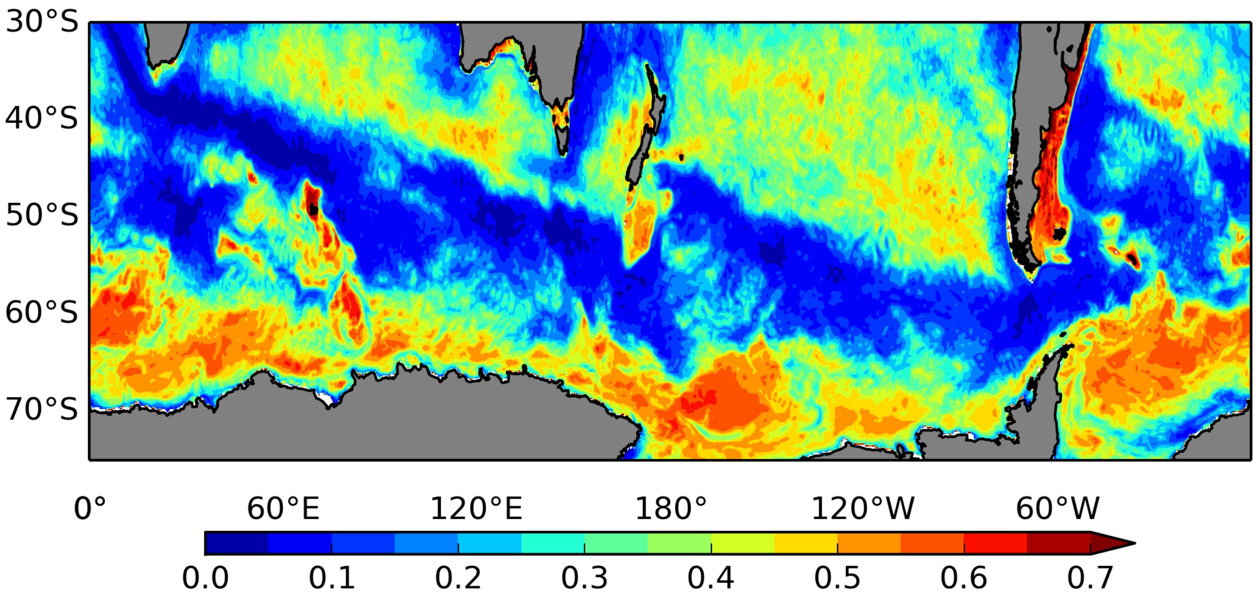

FIG. 18. The kinetic energy ratio $\frac{EKE_{>1}-EKE_{>5}}{EKE_{>1}}$ where $EKE_{>1}$ represents the eddy kinetic energy calculated using the 1-day averaged SOSE velocity and $EKE_{>5}$ using the 5-day averaged SOSE velocity. The eddy kinetic energy is defined as $\overline{\left((u-\overline{u})^2+(v-\overline{v})^2\right)/2}$, where the overbar represents the time average over the 6 years.